A new global C-band vegetation optical depth product from ASCAT: Description, evaluation, and inter-comparison

Xiangzhuo Liu, Wigneron J.-P., Wolfgang Wagner, Frédéric Frappart, Lei Fan, Mariette Vreugdenhil, Nicolas Baghdadi, Mehrez Zribi, Thomas Jagdhuber, Shengli Tao, et al.

A new global C-band vegetation optical depth product from ASCAT: description, evaluation, and inter-comparison

Xiangzhuo Liu[a], Jean-Pierre Wigneron[a,*], Wolfgang Wagner[b], Frédéric Frappart[a], Lei Fan[c], Mariette Vreugdenhil[b], Nicolas Baghdadi[d], Mehrez Zribi[e], Thomas Jagdhuber[f,g], Shengli Tao[h], Xiaojun Li[a], Huan Wang[a,h], Mengjia Wang[i], Xiaojing Bai[j], B. G. Mousa[k], Philippe Ciais[l]

a INRAE, UMR1391 ISPA, Université de Bordeaux, Villenave d'Ornon 33140, France

b Department of Geodesy and Geoinformation, Technische Universität Wien, Vienna 1040, Austria

c Chongqing Jinfo Mountain Karst Ecosystem National Observation and Research Station, School of Geographical Sciences, Southwest University, Chongqing 400715, China

d TETIS, Université de Montpellier, CIRAD/CNRS/INRAE, Montpellier 34093, France

e CESBIO, Université de Toulouse, CNES/CNRS/INRAE/IRD/UPS, Toulouse 31401, France

f Microwaves and Radar Institute, German Aerospace Center (DLR), Münchener Strasse 20, 82234 Weßling, Germany

g University of Augsburg, Institute of Geography, Augsburg 86159, Germany

h Key Laboratory for Earth Surface Processes of the Ministry of Education, Institute of Ecology, College of Urban and Environmental Sciences, Peking University, Beijing 100871, China

i School of Geoscience and Technology, Zhengzhou University, Henan 450001, China

j School of Hydrology and Water Resources, Nanjing University of Information Science and Technology, Nanjing 210044, China

k Department of Mining and Petroleum Engineering, Faculty of Engineering, Al-Azhar University, Cairo 11884, Egypt

l Laboratoire des Sciences du Climat et de l'Environnement, LSCE/IPSL, CEA-CNRS-UVSQ, Université Paris Saclay, Gif-sur-Yvette 91191, France;

*Corresponding Author: J.-P. Wigneron (jean-pierre.wigneron@inrae.fr)

Abstract:

Active microwave measurements have the potential to estimate vegetation optical depth (VOD), an indicator related to vegetation water content and biomass. The Advanced SCATterometer (ASCAT) provides long-term C-band backscatter data at vertical-vertical (VV) polarization from 2007. So far, very few studies have considered retrieving VOD from this active sensor. This study presents a new publicly released global long-term and continuous (2007-2020) C-band VOD dataset retrieved from the ASCAT observations, named the ASCAT INRAE-BORDEAUX or ASCAT IB VOD product. The retrieval algorithm is based on the Water Cloud Model (WCM) including the Ulaby bare soil model. The algorithm takes advantage of a multi-temporal (MT) retrieval method relying on a cost function where constraints to the retrieved parameters are implemented and a reanalysis soil moisture (SM) dataset from ERA5-Land is used as an input. The performance of ASCAT IB VOD was evaluated by inter-comparing it with ASCAT Technische Universität Wien (TUW), the Advanced Microwave Scanning Radiometer 2 (AMSR2), and VOD Climate Archive (VODCA) VOD products (the last two products are estimated from passive microwave observations). Results showed that ASCAT IB VOD presented the highest spatial correlation with aboveground biomass (R~0.83) and with the Global Ecosystem Dynamics Investigation (GEDI) canopy height (R~0.84-0.85). In terms of temporal performance, ASCAT IB VOD had the highest correlation R values with leaf area index (LAI) and Normalized Difference

Water Index (NDWI) in most parts of the globe from 2013 to 2018. This contrasts with AMSR2 VODs which correlated better with Normalized Difference Vegetation Index (NDVI). The new ASCAT-based VOD product on a global scale highlighted the potential benefit of combining active (namely ASCAT) and passive (namely AMSR2) VOD products for vegetation studies.

Keywords: VOD; biomass; vegetation phenology; ASCAT; Active microwave; multi-temporal (MT); AMSR2

1. Introduction:

Microwave vegetation optical depth (VOD) has proven to be a useful indicator for the study of terrestrial ecosystems based on its sensitivity to vegetation biomass as well as water content of vegetation (Chaparro et al., 2019; Frappart et al., 2020; Rodríguez-Fernández et al., 2018a; Vittucci et al., 2019; Wigneron et al., 2021). To date, long-term VOD retrieved from K-, X-, C- and L-band passive microwave brightness temperatures (Kerr et al., 2012; Konings et al., 2017; Liu et al., 2011; Moesinger et al., 2020; Wang et al., 2021a; Wigneron et al., 2017) have been used to monitor the global vegetation biomass changes (Liu et al., 2013), the carbon dynamics in tropical and Siberian regions (Fan et al., 2022; Fan et al., 2019; Wigneron et al., 2020), resilience of the Amazon rainforest (Boulton et al., 2022), vegetation dynamics in drylands over West African Sahel (Tian et al., 2016) and vegetation phenology over the mid- and high-latitudinal Northern Hemisphere (Li et al., 2023). However, some deficiencies, including the discontinuity in time series between observations from satellites and their successor (the Advanced Microwave Scanning Radiometer for EOS, AMSR-E, and the Advanced Microwave Scanning Radiometer 2, AMSR2), as well as data quality issues related to radio frequency interference (Li et al., 2021; Wang et al., 2021b), affect the quality of the above-mentioned passive long-term VOD datasets. Most importantly, a long-term freely available global active VOD product is still lacking and very few studies have focused on this

topic. The development of a new active global product could be very interesting as it could provide useful data to monitor the vegetation characteristics, in a way complementary to passive VODs (Liu et al., 2021b).

The active microwave observations show a different sensitivity to vegetation and soil compared with the passive ones (Link et al., 2021; Prigent et al., 2022). Using a discrete radiative transfer model to simulate the relationship between active and passive signals in three vegetation types (wheat, corn, and forest), Link et al. (2021) found the coupling between active and passive signals decreases with increasing vegetation water content because of the decreasing sensitivities of the radar (active) and radiometer (passive) observations to soil moisture. The sensitivity of the radar systems to SM over vegetation areas decreases more quickly than that of the radiometers due to the two-way vegetation attenuation (forward and backward) (Piles et al., 2015) and active systems are more sensitive to the effects of the vegetation structure (Ferrazzoli et al., 1989; Fung and Eom, 1985; Wigneron et al., 1999). Prigent et al. (2022) found the diurnal and seasonal cycles of backscatter and emissivity collected from Global Precipitation Mission (GPM) at a $1° \times 1°$ resolution tend to be in phase opposition in the tropical forest region, while backscatter and emissivity vary more in phase during the dry season in the less densely forested regions of southeast Amazon. The dissimilar information obtained from active and passive microwave signals motivates us to explore the retrieval of VOD from active microwave observations.

Active microwave data provide complementary observations to passive observations because 1) they are sensitive to specific vegetation characteristics, 2) are less affected by radio interference than passive observations (Liu et al., 2021b) and 3) can also provide long-term records, such as observations from three series of Advanced SCATterometer (ASCAT) Meteorological Operational (MetOp -A/B/C) satellites which start in 2007 and can be extended to the 2020s (Srivastava et al., 2016). Radar observations have been used in many

98 studies for vegetation monitoring (phenology, structure, or productivity) (Canisius et al., 2018;
99 Chang et al., 2022; Hosseini et al., 2015; Meroni et al., 2021; Neumann et al., 2010; Wagner
100 et al., 1999), while studies on active VOD retrievals are scarce and only conducted at the site
101 scale or over small regions (El Hajj et al., 2019a; Grippa and Woodhouse, 2003; Magagi and
102 Kerr, 1997; Quast et al., 2019; Zhou et al., 2022). The first active VOD research at a
103 continental scale (Vreugdenhil et al., 2016) was conducted for assessing the vegetation
104 correction in the Technische Universität Wien (TUW) method of the C-band ASCAT soil
105 moisture retrieval (Wagner et al., 2013). The TUW VOD is retrieved by the change detection
106 method using the Water Cloud Model (WCM) (Attema and Ulaby, 1978). The TUW VOD
107 value is mainly dependent on two parameters (slope and curvature) which are the coefficients
108 of a second-order Taylor expansion function established to describe the angular ASCAT
109 backscatter dependency (Hahn et al., 2017). The preliminary TUW VOD data set did not
110 consider inter-annual variability as the climatology of slope and curvature are computed in the
111 algorithm (Vreugdenhil et al., 2016; Vreugdenhil et al., 2017). With a novel calculation of
112 slope and curvature, the updated TUW VOD can capture vegetation dynamics in Australia
113 (Vreugdenhil et al., 2017). However, it is not yet public and there are few studies on the
114 global assessment of TUW VOD (Teubner et al., 2018; Vreugdenhil et al., 2016).

115 Recently, INRAE-BORDEAUX (IB) developed a new active VOD product from ASCAT in
116 Africa (hereafter ASCAT IB V1 VOD) (Liu et al., 2021b). The algorithm is based on the
117 WCM integrated with the Ulaby bare soil scattering model (Ulaby et al., 1978) as these
118 simple models can be used efficiently to simulate the ASCAT backscattering signals (Lievens
119 et al., 2021; Santoro et al., 2022; Shamambo et al., 2019). To retrieve VOD from the VV
120 polarization and mono-angular (incidence angle at 40°) normalized ASCAT observations, the
121 ERA5-Land soil moisture (SM) dataset was used as an input to the algorithm. The evaluation
122 of ASCAT IB V1 VOD showed a high spatial correlation with Climate Change Initiative

(CCI) and Saatchi above-ground biomass (AGB) (Carreiras et al., 2017; Saatchi et al., 2011; Santoro and Cartus, 2019), with R values generally higher than for ASCAT TUW VOD and C-band passive VOD, namely the Advanced Microwave Scanning Radiometer 2 (AMSR2) and VOD Climate Archive (VODCA) VOD. ASCAT IB V1 VOD was also found to be highly temporally correlated to Moderate Resolution Imaging Spectroradiometer (MODIS) Normalized Difference Vegetation Index (NDVI), Enhanced Vegetation Index (EVI), and leaf area index (LAI). However, the algorithm used in ASCAT IB V1 VOD has been applied globally with imperfect results (Liu et al., 2021a), mainly because the hypothesis that the vegetation scattering parameter (ω) consists globally of two constant values (distinguishing very densely vegetated regions from the other vegetated regions) did not hold.

In the present study, to improve the quality of the global ASCAT IB VOD product, we evaluated the possibility of retrieving VOD and ω simultaneously from the ASCAT normalized backscatter at 40° by adding constraints in the retrieval process. The first constraint was applying a multi-temporal (MT) method which is generally based on the assumption that VOD varies relatively slowly in time as was first developed by Wigneron et al. (2000) for the SM and VOD retrieval algorithm of the Soil Moisture and Ocean Salinity (SMOS) mission (Kerr et al., 2010). This assumption is now widely used in the development of passive VOD retrievals. For instance, in the multi-temporal dual channel retrieval algorithm (MT-DCA), VOD was assumed to be nearly constant between every two consecutive overpasses (Konings et al., 2016). Based on MT-DCA, (Konings et al., 2017; 2016) successfully retrieved VOD and SM from L-band Aquarius (with a seven-day revisit time) and SMAP (with a three-day revisit time). This assumption was also adopted in the different operational VOD and SM retrieval algorithms of the SMOS observations (Al Bitar et al., 2017; Wigneron et al., 2021). Similarly in the active domain, El Hajj et al. (2019a) assumed that VOD remains stable during four consecutive overpasses (18 days) of Sentinel-1

and hence obtained the very first retrievals of VOD from Sentinel-1 images in southern France.

Incorporating a *priori* information into the algorithm is another interesting way to constrain the retrieved parameters. A key feature of the widely used L-band microwave emission of the biosphere (L-MEB) inversion method is integrating a *priori* information into the retrieval (Wigneron et al., 2021; Wigneron et al., 2017). In the SMOS-IC Version 2 algorithm (Wigneron et al., 2021), by using the mean value of VOD retrieved in the previous ten days as a first guess value of VOD for subsequent SM and VOD retrievals, results showed a considerable improvement compared with the preceding versions. In the SMAP official SM baseline algorithm (O'Neill et al., 2015), the MODIS NDVI was converted to vegetation water content and then multiplied by a factor to represent VOD. Based on the optimization of the *a priori* information, Li et al. (2022) developed a new SMAP SM and VOD product (called SMAP-IB) using the L-MEB algorithm. In addition, Wang et al. (2021a) calibrated a relationship between VOD and the Microwave Polarization Difference Index (MPDI) and then used the VOD based on MPDI as the initial value to retrieve X-band VOD from the AMSR2.

In this context, the main objective of this study is to retrieve simultaneously a global ASCAT product including VOD and the vegetation scattering parameter (ω). The retrieval algorithm used the model-based soil moisture (SM) data from the ERA5-Land product as it offers long-term data at a time close to the ASCAT satellite observations owing to its hourly availability. The use of SM data from satellite missions (*e.g.* SMOS, SMAP and AMSR2) is more difficult: observation time is not concurrent to the ASCAT observations; the time period is not long enough; and accuracy may be limited for some satellite products in some areas (Liu et al., 2021b; Xing et al., 2021). To overcome the challenge of retrieving two parameters from a single-angle and polarization ASCAT observation, the concept of “slow VOD time variations”

introduced previously and the *a priori* information obtained from ASCAT IB V1 VOD retrievals over Africa were incorporated into the algorithm. Similar to previous VOD assessment studies (Chaparro et al., 2019; Li et al., 2021; Liu et al., 2021b), thirteen years of global ASCAT IB VOD (2007-2020) were retrieved and evaluated using different AGB, tree height and optical vegetation index products. The key characteristics of the global ASCAT IB VOD product are illustrated by performing comparisons with ASCAT TUW VOD and two other passive C-band VOD products from the AMSR2 satellite, namely AMSR2 VOD and VODCA VOD.

2. Data description

2.1 ASCAT backscatter

The ASCAT sensors are equipped with fan-beam (mid, fore, and aft) antennas which conduct VV backscatter observations with incidence angles varying from 25 to 65 degrees at a carrier frequency of 5.255 GHz (C-band) covering two 550 km wide swaths separated by a gap of about 360 km with a 30–50 km spatial resolution and twice a day temporal resolution (Figa-Saldaña et al., 2014). In the present study, we used the backscatter measurements normalized at the standard reference angle (40°) and the historically wettest measurements (referred to as wet reference), which were extracted from the ASCAT Soil Moisture near-real time (NRT) product at 12.5 km Swath Grid. This product provides 15 scene acquisitions per day and covers the globe approximately every two days. The stack of the ASCAT backscatter data used in this study consisted of all data acquired by MetOp-A descending orbits (9:30 am) from 2007 to 2020. We used data measured at morning because vegetation water stress is typically lower in the morning making "morning" VOD better suited for monitoring biomass (Frappart et al., 2020; Liu et al., 2021b). The data with good quality (probability flags for frozen soil and snow equal to zero, topographic complexity flags and wetland probability flags lower than 30% and 10%, respectively) were resampled to a 0.25° grid (~ 25 km × 25

198 km) by the inverse distance weighting algorithm (Lievens et al., 2017). The ASCAT data is
199 freely available at https://archive.eumetsat.int/.

200 **2.2 ERA5-land data**

201 In this study, we used the 0–7 cm SM and soil temperature (ST) datasets of ERA5-Land
202 (Muñoz-Sabater et al., 2021). This dataset is on a 0.1-degree grid with hourly time steps. The
203 new surface model (Carbon Hydrology-Tiled ECMWF Scheme for Surface Exchanges over
204 Land) used in ERA5-Land is able to better simulate the SM dynamics than the older scheme
205 (Wagner et al., 2022). The evaluation of ERA5-Land SM also shows good performance on the
206 global scale (Beck et al., 2020; Chen et al., 2021; Lal et al., 2022; Muñoz-Sabater et al.,
207 2021). More importantly, as the ERA5-Land does not assimilate land surface observations
208 (whereas ERA5 assimilates the ASCAT SM), ERA5-Land SM and the ASCAT backscatter
209 measurements can be treated as quasi-independent variables (Wagner et al., 2022). In the
210 present study, ERA5-Land SM is used as an input to the WCM model to retrieve ASCAT IB
211 VOD, and ERA5-Land ST is used for simulating the Ulaby bare soil model parameters.
212 ERA5-Land SM and ST were aggregated to the 0.25° grid using area-weighted averaging, and
213 then temporally matched with the ASCAT descending (~9:30 local time) observations.

214 **2.3 Vegetation variables for evaluating VOD**

215 Three kinds of vegetation variables widely used in VOD evaluation (Grant et al., 2016; Li et
216 al., 2021; Rodríguez-Fernández et al., 2018b; Tian et al., 2016) were used to evaluate the
217 retrieved ASCAT IB VOD: AGB, canopy height, and optical vegetation indices. The rationale
218 for using those parameters is that 1) there is no consensus on *in-situ* VOD reference values, so
219 proxies of VOD as vegetation height and vegetation biomass are often used to evaluate the
220 performance of the VOD retrieval algorithms (Li et al., 2022; Li et al., 2021); 2) VOD can
221 provide information on AGB at the inter-annual scale and on the vegetation water status at the

seasonal scale (Lyons et al., 2021; Wang et al., 2023). Since total vegetation biomass (AGB) is generally well related to vegetation height (Asner et al., 2012), utilizing canopy height may confirm the anticipated relationship between VOD and AGB. We also refer the reader to the inter-comparison study of nine commonly used VOD for more details (Li et al., 2021).

2.3.1 AGB datasets

Three AGB products, the Saatchi AGB in 2015 (Carreiras et al., 2017; Saatchi et al., 2011), the Climate Change Initiative (CCI) AGB dataset version 1 in 2017 (Santoro and Cartus, 2019) and the Global Ecosystem Dynamics Investigation (GEDI) L4B AGB in 2020 (Dubayah et al., 2022), were used to evaluate the ability of ASCAT IB VOD to monitor AGB. Those three datasets are all at 1-km spatial resolution and were resampled to the 0.25° grid by spatial averaging.

2.3.2 Canopy height datasets

Two canopy height products (Lang et al., 2022; Potapov et al., 2020) used in this study were derived from the GEDI LIDAR measurement. The product developed by Potapov et al. (2020) is produced by extrapolating the GEDI footprint-level forest canopy height to a 30 m spatial resolution map using a regression tree algorithm and Landsat analysis-ready data for the year 2019. Lang et al. (2022) used the GEDI Level 1B waveforms and Bayesian deep learning algorithm to develop a global 0.5° resolution canopy height map, which has a lower root mean square error (RMSE = 2.7m) than the product (RMSE = 6.6m) from Potapov et al. (2020).

2.3.3 Optical vegetation indices datasets

Three vegetation indices (VIs) products, the 10-day NDVI and LAI data from Copernicus Global Land Service (CGLS) (https://land.copernicus.eu/global/) and 8-day Normalized Difference Water Index (NDWI) calculated from the MODIS MOD09A1 product (Gu et al., 2008), were used to assess the temporal variations in ASCAT IB VOD. LAI and NDVI are

246 good proxies of phenology and vegetation greenness. NDWI represents the vegetation water
247 dynamics which is expected to be important in terms of temporal changes. Therefore, those
248 three VIs can be used to test the ability of ASCAT IB VOD to monitor the seasonal and
249 interannual variations of vegetation phenology and vegetation water status. After quality
250 control, the dataset was resampled to a spatial resolution of a 0.25° grid (Fuster et al., 2020).

251 **2.4 Other C-band VOD products**

252 To better illustrate the performance of the ASCAT IB VOD product, we inter-compared it
253 with three other C-band VOD products, namely ASCAT TUW, AMSR2 and VODCA VOD.
254 ASCAT TUW VOD was provided by Vreugdenhil et al. (2016). TUW VOD is calculated
255 from the loss in sensitivity to soil moisture (i.e., attenuation of the bare soil backscatter). The
256 sensitivity is calculated as the difference between the wet and dry reference, and more details
257 on the product are given in (Vreugdenhil et al., 2016; Vreugdenhil et al., 2017). AMSR2 and
258 VODCA VOD can be freely downloaded at the Goddard Earth Sciences Data and Information
259 Services Center (GES DISC) website and the Zenodo repository (Moesinger et al., 2020).
260 These two products are retrieved from the passive sensor AMSR2 (providing data from July
261 2012) but with different algorithms. The AMSR2 VOD retrieval algorithm is based on the
262 Land Parameter Retrieval Model (LPRM) version 5 (Owe et al., 2008), while VODCA VOD
263 is retrieved via the LPRM version 6 and then a cumulative distribution function (CDF)
264 matching technique is used to scale VOD to the AMSR-E VOD (Moesinger et al., 2020). The
265 key differences between those three products and ASCAT IB VOD are presented in the
266 discussion section.

267 **2.5 Ancillary datasets**

268 This study also utilized several ancillary datasets, including ISRIC SoilGrids250m data
269 (Hengl et al., 2017), Digital Elevation Model (DEM)-related data (Danielson and Gesch,

2011), and MODIS land cover map (Sulla-Menashe et al., 2019). The SoilGrids250m dataset provides global standard numeric soil properties at seven standard depths with a 250 m spatial resolution. DEM-related data were calculated from the 1km Global Multi-resolution Terrain Elevation Data 2010 by using the System for Automated Geoscientific Analyses (SAGA) GIS software (Conrad et al., 2015). The SoilGrids250m (15 types, in Table S1), and DEM-related (9 types, in Table S2) data were used in the estimation of the soil parameters of the Ulaby linear model (see Section 3.1). As several previous studies showed that VOD varies as a function of the land cover (Li et al., 2021; Vreugdenhil et al., 2016), the land cover map extracted from the MODIS MCD12Q1 product based on the International Geosphere-Biosphere Programme (IGBP) scheme was used to analyze the different VOD products.

3. Methodology

The ASCAT IB retrieval approach is illustrated in the flowchart of Fig.1. The retrieval model is based on a vegetation backscatter model (Water Cloud Model) integrated with the Ulaby bare soil model (Section 3.1). Instead of the common procedure in which VOD and SM are retrieved simultaneously, which may lead to an ill-posed problem (Wigneron et al., 2000), we focused on retrieving the two vegetation parameters, VOD and vegetation scattering parameter (ω), which can be assumed to be relatively constant over a short time-window, while model-based dynamic SM data is used as an input in the retrieval algorithm. One prototype study undertaken to retrieve VOD from AMSR2 in Africa supports the validity of this idea (Wang et al., 2021a). The estimation of the Ulaby linear model parameters is described in Section 3.2. The retrieval of the VOD and ω from the integrated retrieval model is presented in Section 3.3. The methods implemented to quantify the performance of ASCAT IB VOD and to qualify the ω parameter are described in Section 3.4.

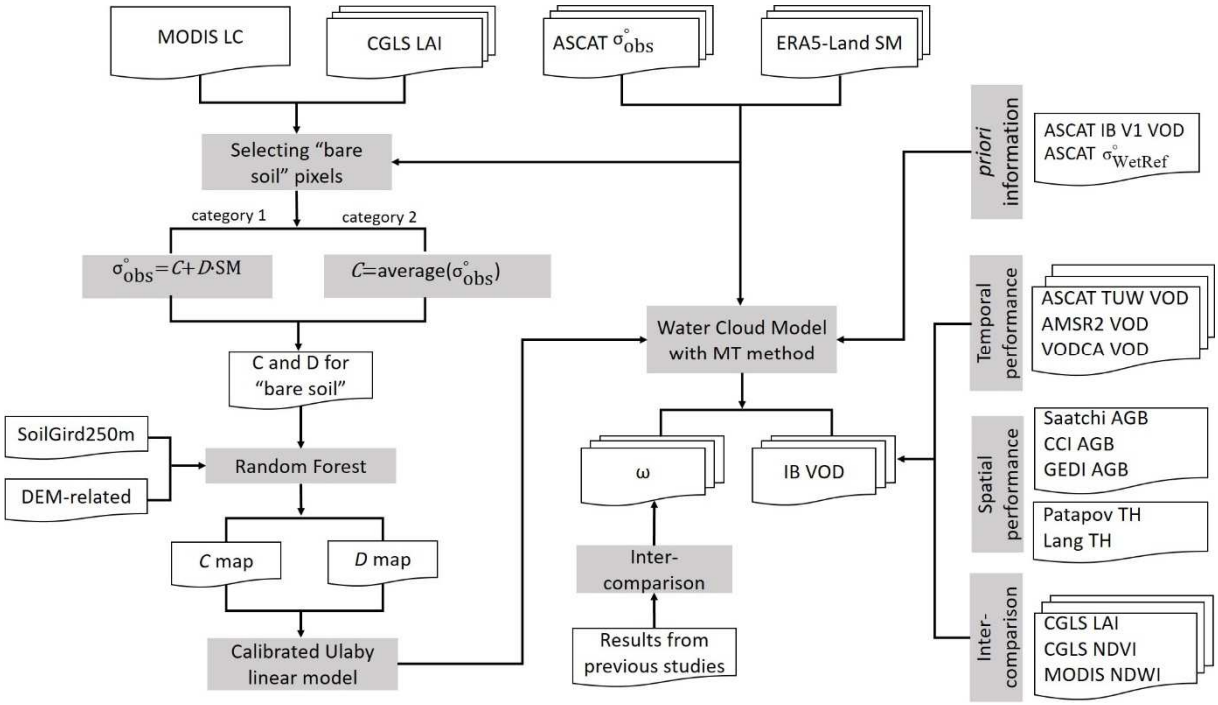

Fig. 1. Flowchart presenting the development and assessment of global ASCAT IB VOD.

3.1. Vegetation backscatter model

The radar backscatter from vegetation was described by the Water Cloud Model (WCM) (Attema and Ulaby, 1978). The sensor-received backscattering coefficient (σ°_{obs}, in m^2/m^2) at the incidence angle θ (40° in this study) can be denoted as a combination of two components: the direct vegetation backscatter signal (σ°_{veg}, in m^2/m^2) and the backscatter from the soil surface (σ°_{soil}, in m^2/m^2) attenuated by the vegetation canopy (γ^2, called the two-way vegetation attenuation factor). This leads to the following equations:

$$\sigma^\circ_{obs}=\sigma^\circ_{veg}+\gamma^2\sigma^\circ_{soil} \quad (1)$$

$$\sigma^\circ_{veg}=\omega\cdot\cos\theta\cdot(1-\gamma^2) \quad (2)$$

$$\gamma^2=\exp(-2\cdot\tau/\cos\theta) \quad (3)$$

where ω is the vegetation scattering parameter related to the single scattering albedo, and τ is the vegetation optical depth (VOD).

A simple linear approach (Eq. (4)) (Ulaby et al., 1978) was used to model the bare soil backscatter (σ°_{soil}, in dB) as a function of soil moisture (SM, in m^3/m^3):

$$\sigma^{\circ}_{soil(dB)}=10\cdot\log_{10}\sigma^{\circ}_{soil(m^2/m^2)}=C+D\cdot SM \quad (4)$$

where C is the radar backscatter of the very dry bare soil, D represents the radar backscatter sensitivity to soil moisture changes, and SM comes from the ERA5-land SM product.

The Eqs. (2)- (4) were finally inserted into Eq. (1) to express σ°_{obs} as a function of vegetation optical depth (τ):

$$\sigma^{\circ}_{obs}=\omega\cdot\cos\theta\cdot(1-\exp(-2\cdot\tau/\cos\theta))+\exp(-2\cdot\tau/\cos\theta)\cdot 10^{0.1\cdot(C+D\cdot SM)} \quad (5)$$

3.2 Calibration of the model parameters

The soil-vegetation radar model in Eq. (5) contains three parameters (ω, C and D) that needed to be calibrated on each pixel in space and time. As there are no "true" VOD samples, the three parameters cannot be calibrated at the same time. In this study, we calibrated the bare soil parameters (C and D) and then retrieved ω and VOD simultaneously.

The soil parameter calibration consisted of three steps (1) selecting so-called "bare soil" pixels globally where vegetation effects can be neglected during a specific period (which varies over each pixel) (2) computing the C and D parameters over the "bare soil" pixels during that specific period (3) training machine learning models by using the retrieved C and D values over "bare soil" pixels obtained in the step (2) and then estimating the two parameters (C and D) globally. These three steps are detailed below:

Step1: Globally selecting the "bare soil" pixels based on LAI and land cover data. Two kinds of "bare soil" pixels can be identified: i) vegetation-free pixels during the entire year (desert area), and ii) pixels with sparse vegetation (LAI<0.5) seasonally. Some "bare soil" pixels have very low moisture condition (< 0.05 m^3/m^3) and almost stable σ°_{obs}. In those pixels, only C can be calculated. Therefore, we divided the "bare soil" pixels into two categories, namely category 1: where soil moisture and σ°_{obs} show a significant correlation; category 2: where soil moisture is very low and there are very low time variations in σ°_{obs}.

Step2: calculating the parameters *C* and *D* over the "bare soil" pixels. For the pixels in category 1, the *C* and *D* values were obtained with linear fitting on Eq. (4). For the pixels in category 2, only the *C* value can be computed, and it was estimated from the averaged σ°_{obs}. At the same time, the corresponding soil properties (Table S1) and DEM-related (Table S2) data were extracted.

Step3: estimating *C* and *D* globally. The pixels in step 2 were used to train two random forest (RF) regression models, in which the parameters *C* and *D* computed over the "bare soil" pixels were treated as the target and the soil properties (Table S1) and DEM-related (Table S2) data were selected as the predictors. More details about the implementation of the RF model are presented in Appendix A. Then, the selected global predictors were used as input to the trained RF models to estimate *C* and *D* globally.

Two years (2015-2016) of ASCAT σ°_{obs} and ERA5-Land SM were used to select the "bare soil" pixels. For more details about each step, readers can refer to the same calibration work done in Africa (Liu et al., 2021b).

3.3 Retrieval of VOD and ω

The simultaneous retrieval process of two variables, VOD and ω, was performed by using a cost function (*CF*) (Eq. (6)). *CF* integrates the squared weighted differences between the backscatter simulations (σ°_{sim}) and the observations (σ°_{obs}), taking into account the constraint information on the retrieved model parameters (Wigneron et al., 2007). This strategy was also implemented in the development of SMOS IC V2 and SMAP IB (Li et al., 2022; Wigneron et al., 2021).

$$CF=\frac{\sum(\sigma^{\circ}_{obs}-\sigma^{\circ}_{sim})^2}{\mathrm{StdDev}(\sigma^{\circ})^2}+\sum_{i=1}^{2}\frac{\left(P_i^{ini}-P_i^{*}\right)^2}{\mathrm{StdDev}(P_i)^2} \quad (6)$$

where the sum of the differences between observed (σ°_{obs}) and simulated (σ°_{sim}) backscattering coefficient is computed from VV polarization observations over a *w*-day window. In this window, the value of retrieved P_i^*(VOD* and ω^*, respectively for i = 1, 2) are time-invariant. StdDev(σ°) is the standard deviation associated with σ°_{obs}. P_i^{ini} (VOD^{ini} and ω^{ini}, respectively for i = 1, 2) is the initial value of VOD or ω in the retrieval process and corresponds to a constraint information (or "*priori* information") estimate; StdDev(P_i) is the standard deviation associated with this estimate.

Two sources of constraint information were used in the retrieval algorithm: (1) the ASCAT IB V1 VOD developed in Africa (Liu et al., 2021b) was used to estimate the *a priori* information on VOD, and (2) the wet reference of the ASCAT observations was used to estimate the *a priori* information on ω. Specifically, due to the diversity of the vegetation conditions in Africa, the VOD^{ini} and StdDev(VOD) parameters used in Eq. (6) were simply estimated for the forest and non-forest regions in Africa. In this study, VOD^{ini} was set to 0.87 and 0.16 for forest and no-forest pixels, respectively. StdDev(VOD) was set to 0.40 for forest pixels and 0.15 for no-forest pixels. According to the definition of ω, the ω^{ini} and StdDev(ω) parameters were calculated from the ASCAT wet reference (σ°_{WetRef}) data which is computed from the maximum backscattering coefficient for each pixel during the peak growth season (Fig. 1 in Steele-Dunne et al. (2019) and Fig. 2 in Vreugdenhil et al. (2016)) or during times with high values of ERA5-Land SM (Fig. S1). σ°_{WetRef} is provided over each pixel and is almost constant on a daily basis. The yearly mean value of σ°_{WetRef} in each pixel was used to estimate ω^{ini}. Like the calculation of StdDev(VOD), StdDev(ω) was estimated from the yearly mean value of σ°_{WetRef} over the forested and non-forested areas. It was set to 0.01 for the forested areas and 0.03 for the non-forested areas.

In order to ensure a good quality of P_i^*(VOD and ω) and to consider that P_i^* did not change much over the period of *w*-days, the *w* value cannot be too small or too large (Wigneron et al.,

2021). An 18-day window was used in this study. This window size allows for robust results with more than three consecutive observations and it corresponds to the time-period used for Sentinel-1 VOD (El Hajj et al., 2019a). We also checked that this window size led to the best results when evaluating the performance of ASCAT IB VOD against AGB (Table S3).

3.4. Evaluation metrics for ASCAT IB retrievals assessments

Evaluating the ASCAT IB retrievals, we mainly focused on the VOD parameter as there are few studies evaluating the ω parameter at a large scale (Du et al., 2016; Fernandez-Moran et al., 2016; Konings et al., 2017; Vittucci et al., 2017). As in (Li et al., 2021), the global ASCAT IB VOD retrievals were evaluated in time and space. For the temporal performance, the Pearson correlation coefficient (R) between optical vegetation indices (i.e., LAI, NDVI and NDWI and ASCAT IB VOD was calculated. To evaluate ASCAT IB VOD in terms of spatial performance, we estimated the spatial correlation between ASCAT IB VOD and different AGB products (Eq. (7)). Meanwhile, the spatial correlation between VOD-predicted-AGB and AGB was also computed: the aim is to evaluate the performance of ASCAT IB VOD and other VOD in estimating AGB. To compute the VOD-predicted AGB as a function of ASCAT IB VOD, two functions (Eq. (8)-(9)) were chosen to fit the relationship between VOD and AGB (Li et al., 2021; Wang et al., 2021a). The root mean square deviation (RMSE) between VOD-predicted-AGB and AGB was also calculated (Eq. (10)). The same calculation was also done for ASCAT IB VOD and different canopy height products.

$$\mathrm{R} = \frac{\sum_{\mathrm{i}=1}^{n}(\mathrm{VOD_i} - \overline{\mathrm{VOD}})(Y_\mathrm{i} - \bar{Y})}{\sqrt{\sum_{\mathrm{i}=1}^{n}(\mathrm{VOD_i} - \overline{\mathrm{VOD}})^2}\sqrt{\sum_{\mathrm{i}=1}^{n}(Y_\mathrm{i} - \bar{Y})^2}} \quad (7)$$

$$Y = \frac{\mathrm{a}}{1 + \exp\big(-\mathrm{b} * (\mathrm{VOD} - \mathrm{c})\big)} + \mathrm{d} \quad (8)$$

$$Y = \mathrm{a} * \exp(\mathrm{b} * \mathrm{VOD}) + \mathrm{d} \quad (9)$$

$$\mathrm{RMSE} = \sqrt{\frac{\sum_{i=1}^{n}(y_i - Y_i)^2}{n}} \quad (10)$$

where Y is AGB or canopy height, a, b, and c are best-fit parameters, y is the predicted AGB or predicted canopy height, n is the valid number of pixels.

The spatial and temporal performance of three other C-VOD products were also evaluated for inter-comparing with ASCAT IB VOD. In order to keep consistency for each product, the following criteria were used: 1) for each product, we used VOD data from the same year (or close in time) as the vegetation-related proxies; 2) since the VODCA data set is only available until 2018 and AMSR2 provides data from July 2012, the temporal evaluation was made from 2013 to 2018; and 3) over each pixel and each year, the number of VOD data should be larger than 60 per year to avoid statistical under-representation. The retrievals of the VOD and ω parameters were also analysed considering different classes of vegetation types defined by the MODIS IGBP classification scheme.

4. Results

4.1 Calibration results of the *C* and *D* parameters

The "bare soil" pixels used for the computation of the *C* and *D* parameters of the Ulaby bare soil scattering model (Eq. (4)) are presented in Fig. 2. The red pixels, corresponding to the "bare soil" regions where the backscatter signals were observed in a prolonged state of dryness, are in the desert area. For the blue pixels in non-desert regions, the *C* and *D* values were computed from Eq. (4), keeping only pixels where the correlation coefficient (R) is larger than 0.25. Those pixels are mainly distributed in the north, center, and south of Africa, the south of Australia, south of Southern America, Central Asia, and the western regions of the United States. The main land cover types associated with the blue pixels are grassland, cropland, and open shrubland which have a clear seasonality. As a result, the *C* value could be

estimated over 23,482 pixels and the *D* value over 24,205 pixels. The corresponding soil properties (18 types) and terrain-related indexes (9 types) of these pixels were extracted, and then they were used as predictors to train two random forest models (referred to as the *C* and *D* models, respectively) for simulating, separately, the *C* and *D* parameters at the global scale.

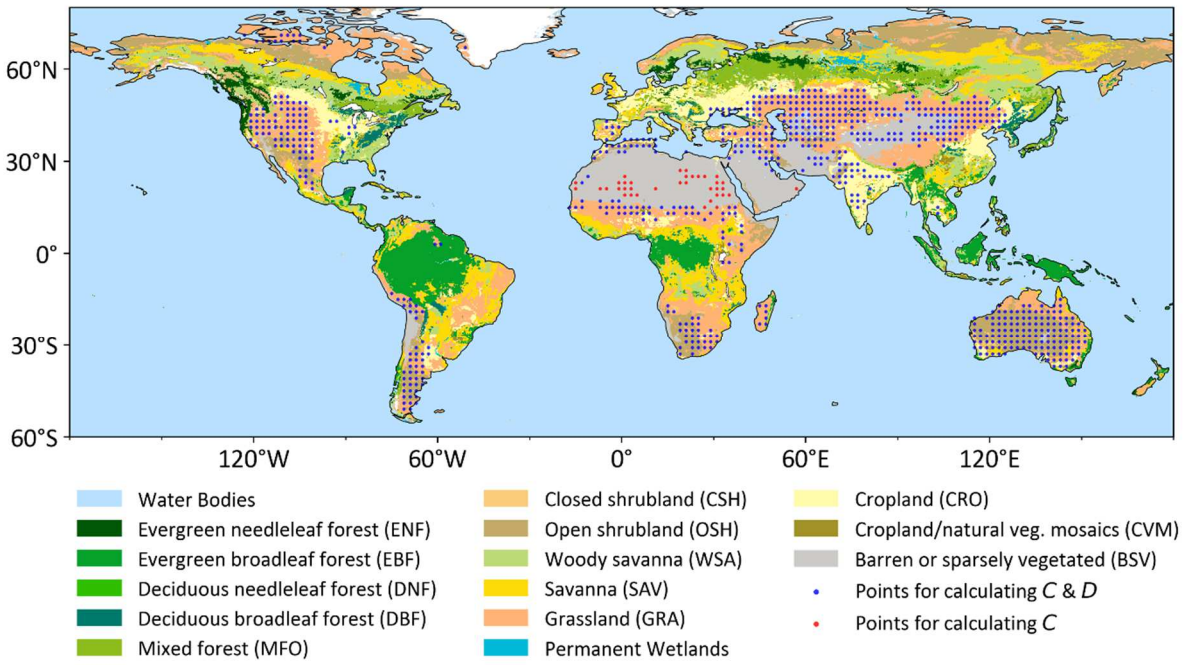

Fig.2. Spatial distribution of the "bare soil" pixels (represented by points) and MODIS IGBP land cover map. The "bare soil" pixels are shown in a 2° × 2° grid if the total number of *C* or *D* pixels is larger than six.

In total, 18 predictor variables were selected to train the *C* model and 19 predicator variables were selected to train the *D* model after applying the recursive feature elimination (RFE) method. Fig. 3 (a-b) shows the variable importance of each *C* and *D* model. Soil property indices (group SPI) played a key role in estimating the target variables in both the *C* and *D* models, with a total importance of 79.39 % and 65.67 %, respectively. The soil organic carbon density (Ocdens) ranked first in SPI for both models. The terrain-related features (group TI) contributed more in the *C* model than in the *D* model, which is consistent with the results obtained in Africa (Liu et al., 2021b).

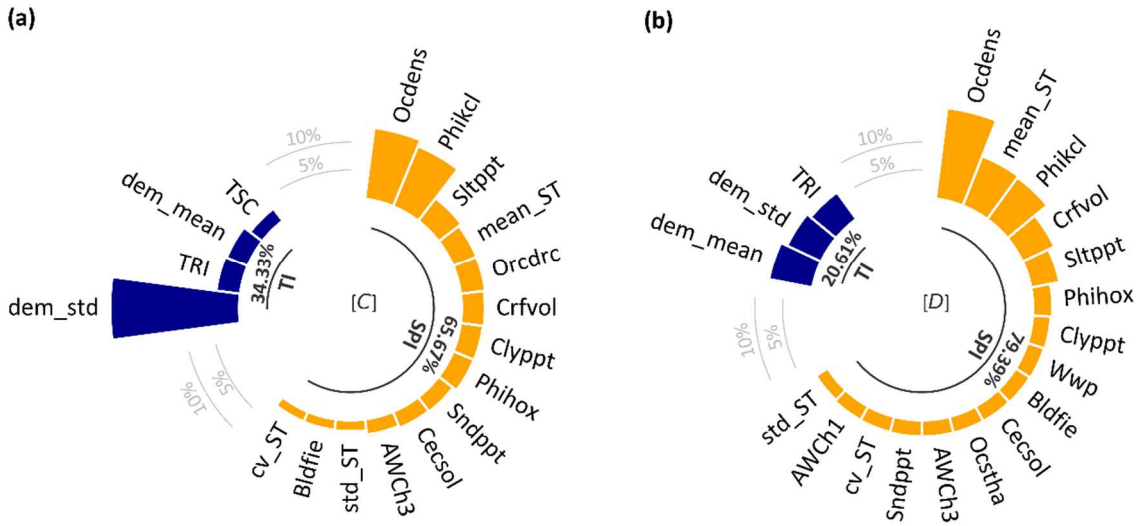

441

442 **Fig.3.** Predictive variable importance of the *C* (a) and *D* (b) model values. SPI and TI mean
443 soil property indices (in orange) and terrain-related feature variables (in dark blue),
444 respectively. The definition of each variable is given in Table S1 and S2.

445 The results of the 10-fold cross-validation of two RF models trained by the selected indices
446 (Fig. 4) are better than those obtained in Africa (Liu et al., 2021b). For the *C* model, R^2
447 increased from 0.85 to 0.87, and RMSE decreased from 1.31 dB to 0.97 dB. The R^2 metric of
448 the *D* model improved from 0.61 to 0.79, but the RMSE showed a slight increase (from
449 2.37 dB/ $m^3 \cdot m^{-3}$ to 2.43 dB/ $m^3 \cdot m^{-3}$). The overestimation of the lower values and
450 underestimation of the higher values obtained in Africa still occurred for the two models
451 calibrated here at the global scale. This is likely due to the limitation of the RF regression
452 model that cannot be extrapolated; namely when the range of the test fold is not included in
453 the training fold, values beyond the range of the training data set will be overestimated or
454 underestimated.

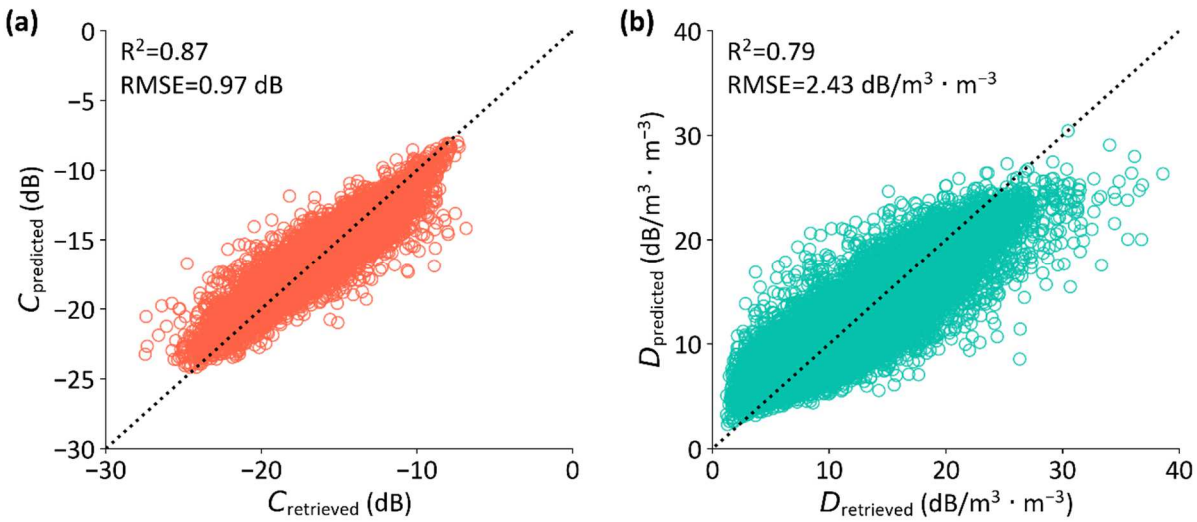

455

456 **Fig. 4.** Performance of the *C* (a) and *D* (b) soil model based on the 10-fold cross-validation.

457 The spatial patterns of the global predicted *C* and *D* parameters are illustrated in Fig. 5. The
458 5th–95th percentiles of the *C* and *D* values among all pixels varied from -18.05 dB to -11.82
459 dB, and from 5.12 dB/ $m^3 \cdot m^{-3}$ to 13.97 dB/ $m^3 \cdot m^{-3}$, respectively. These values are in the
460 usual range for C-band SAR observations (Baghdadi et al., 2008; Baghdadi et al., 2016;
461 Verhoest et al., 2008). The distribution of the *D* values is more discrete than that of the *C*
462 values. The pixels with a value ranging from -15 dB to -10 dB account for 76.20 % of the
463 pixels in the *C* map, while 66.62 % of them are concentrated in the range of -15 dB to -12.5
464 dB. Comparatively, 75.26 % of the pixels have a *D* value in the 5-10 dB/ $m^3 \cdot m^{-3}$ range and
465 are evenly distributed in 5-7.5 dB/ $m^3 \cdot m^{-3}$ (accounting for 38.79 %) and 7.5-10 dB/
466 $m^3 \cdot m^{-3}$ (accounting for 36.46 %). In addition, the distribution of the pixels with a *C* value
467 lower than -15 dB in the *C* map matches well with the distribution of pixels with a *D* value
468 larger than 10 dB/ $m^3 \cdot m^{-3}$ in the *D* map, especially in South and North America, Eastern
469 Europe, and Central Asia. Considering each IGBP landcover (Fig. 5 (c)), we can see that the
470 *C* and *D* parameters have a wide range of values in the low vegetation areas. A wide range of
471 *C* values can also be found in mixed forest (MFO). The median *C* values were similar across

all vegetation types, while the median D values varied across the different land cover types. More details about the statistical description of C and D are given in Appendix Table 1-3.

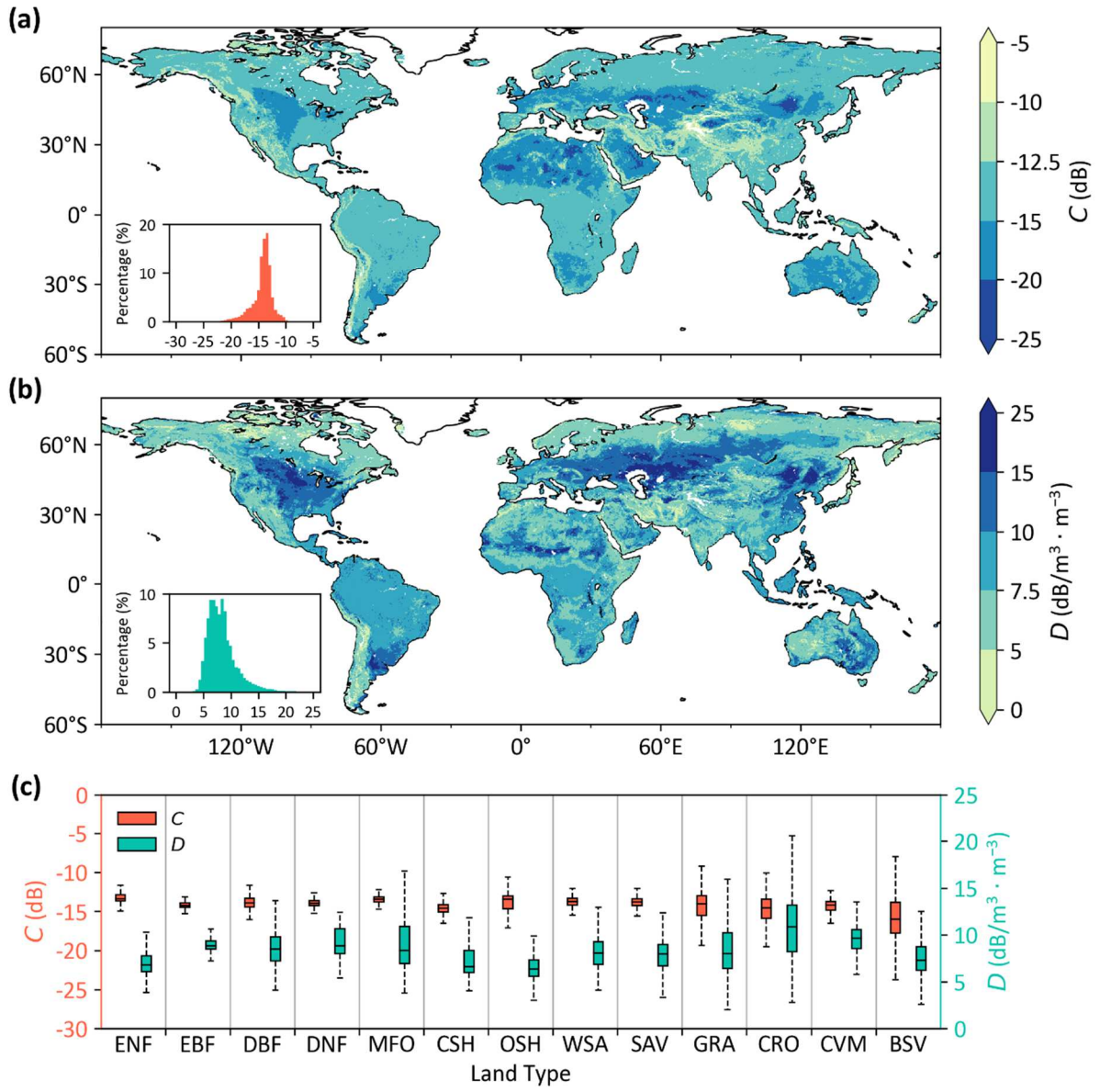

Fig. 5. Global maps of the C (a) and D (b) soil model parameters estimated from the RF models and (c) their boxplots for different IGBP land types.

4.2 Vegetation scattering parameter (ω) retrieval

A global map of the thirteen-year time-average retrieved ω (based on w=18 days) is shown in Fig. 6 (a). The highest values ($\omega > 0.32$) were obtained in Western Australia, northern Mexico, northwest Canada, eastern Lena River in Russia, southern Somalia, western Arabian

Peninsula, southwest Iran, and northern Pakistan. Those regions are in areas with complex terrain of hills and gullies. High values of ω were also retrieved in most pixels of the tropical regions. A clear gradient of increasing average ω value from north to south can be seen across the Sahel. The maximum values of ω reach up to 0.97, and the pixels with values in the range of 0.08-0.32 account for 97.36 % of all pixels. A boxplot of ω for each land cover type sorted by decreasing median values are shown in Fig 6 (c). Evergreen broadleaf forests (EBF) have the highest ω values, which is consistent with previous results from a calibration of the ω values over southern France (Shamambo et al., 2019). Interestingly, high ω values were obtained in the Cropland/Natural vegetation mosaics (CVM) where roughly half of the pixels (53.48%) have a value greater than 0.24. The standard deviation of the ω value in low vegetation is larger than that in the forest and woody savannas areas.

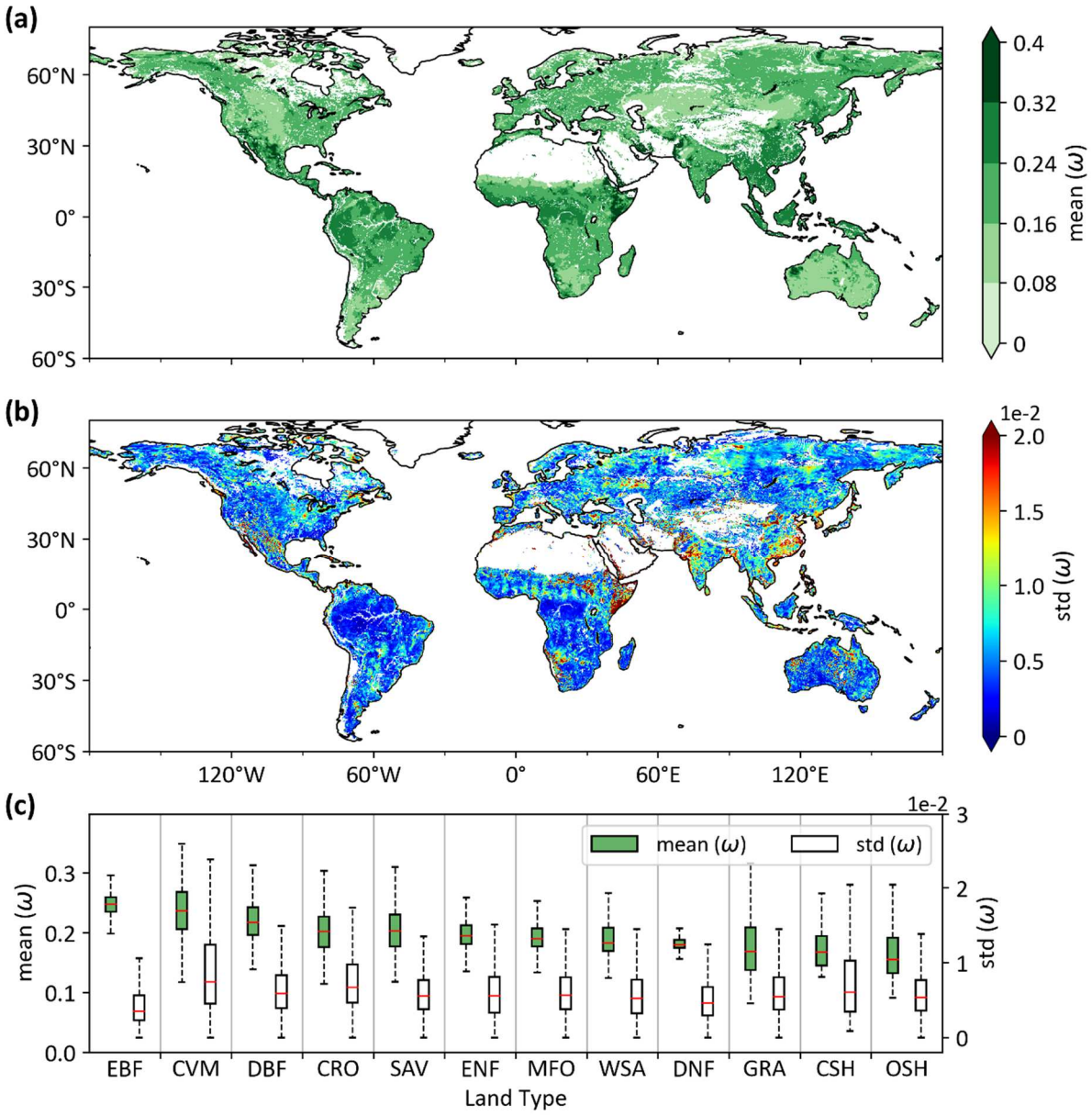

Fig. 6. Global distribution of (a) temporal average and (b) standard deviation of the retrieved ω parameter from 2008 to 2020, and (c) the mean value per vegetation type ordered by decreasing values and the corresponding standard deviation.

4.3 ASCAT IB VOD evaluation

4.3.1 Global spatial patterns

The spatial distribution of the four VODs (Fig. 7) shows that the passive VOD products (AMSR2 VOD and VODCA VOD) have a larger coverage as the active VOD products (ASCAT IB VOD and ASCAT TUW VOD) failed to obtain values in some areas (algorithm

failure). In the ASCAT IB VOD retrieval algorithm, we did not perform VOD retrievals in bare soil areas when the bare soil fraction is greater than 99 % and in pixels where we failed to simulate the bare soil backscatter (*i.e.* when the simulated bare soil backscatter value is larger than the observed backscatter value). The retrieval of TUW VOD was not performed when the difference between the wet and dry reference exceeds the maximum range in the backscatter signal over bare soils (Vreugdenhil et al., 2016). The maximum values of all the four VODs were retrieved in the tropics with VOD ~ 1.2 for AMSR2 and ASCAT TUW VOD, ~ 1.0 for ASCAT IB VOD, and ~ 0.75 for VODCA VOD. The two passive VOD products (AMSR2 and VODCA) have a similar spatial distribution, with higher values in the boreal forests similar to those in the tropical region because they are retrieved from the same sensor (AMSR2) but with a different version of the algorithm. The zonal averaged VOD per latitude (Fig. 7 (e)) shows two peaks at the latitudes of ~ 0°N and ~ 60°N for all three VODs, except for ASCAT TUW VOD. At the latitude of ~ 0°N corresponding to regions of dense tropical forests, both ASCAT VODs decrease rapidly from north to south, while both AMSR2 VODs show a plateau at ~ 0°N and decrease from a latitude of about 13°S.

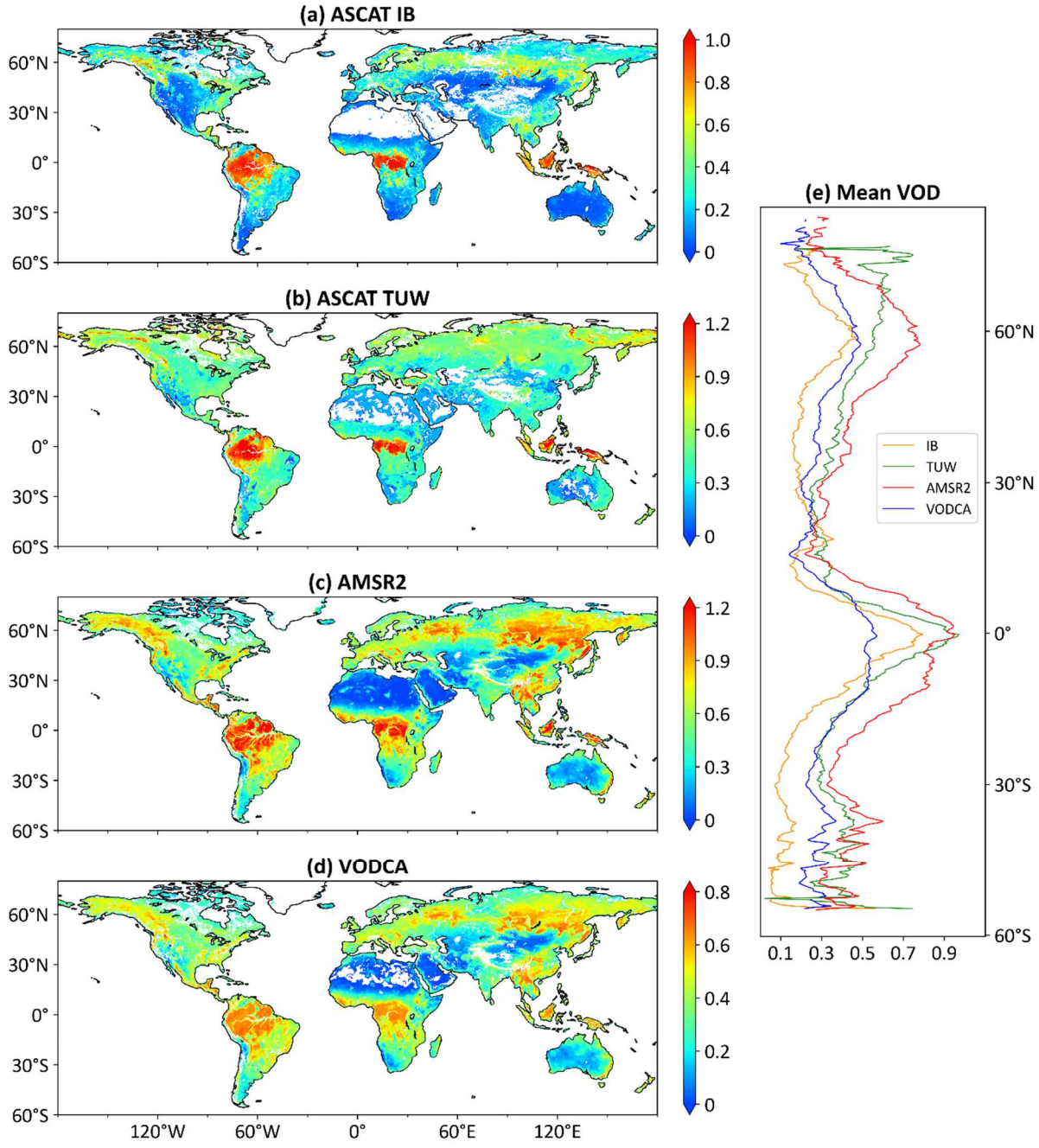

516

517 **Fig. 7.** Global distribution of time-averaged VOD maps over the period from years 2013-
518 2018, (a) ASCAT IB, (b) ASCAT TUW, (c) AMSR2, (d) VODCA and (e) corresponding
519 zonal average.

520 In order to quantitatively describe the differences among the four VODs, we computed the
521 spatial correlation and residuals of the relationship between ASCAT VOD IB and the three
522 other VOD products (Fig 8). ASCAT IB VOD has the highest correlation with AMSR2 VOD,

followed by VODCA VOD and ASCAT TUW VOD. AMSR2 and VODCA VOD show a piecewise linear correlation with ASCAT IB VOD, while the correlation between TUW VOD and ASCAT IB VOD is quite low when the ASCAT IB VOD value is lower than 0.6. The residual plots show that the value of ASCAT IB VOD is lower than that of AMSR2 VOD in almost all pixels. Compared with VODCA VOD, ASCAT IB VOD values are larger when their values exceed 0.8. ASCAT IB VOD values are lower than the ASCAT TUW VOD values except for values in the range of 0.7-0.8.

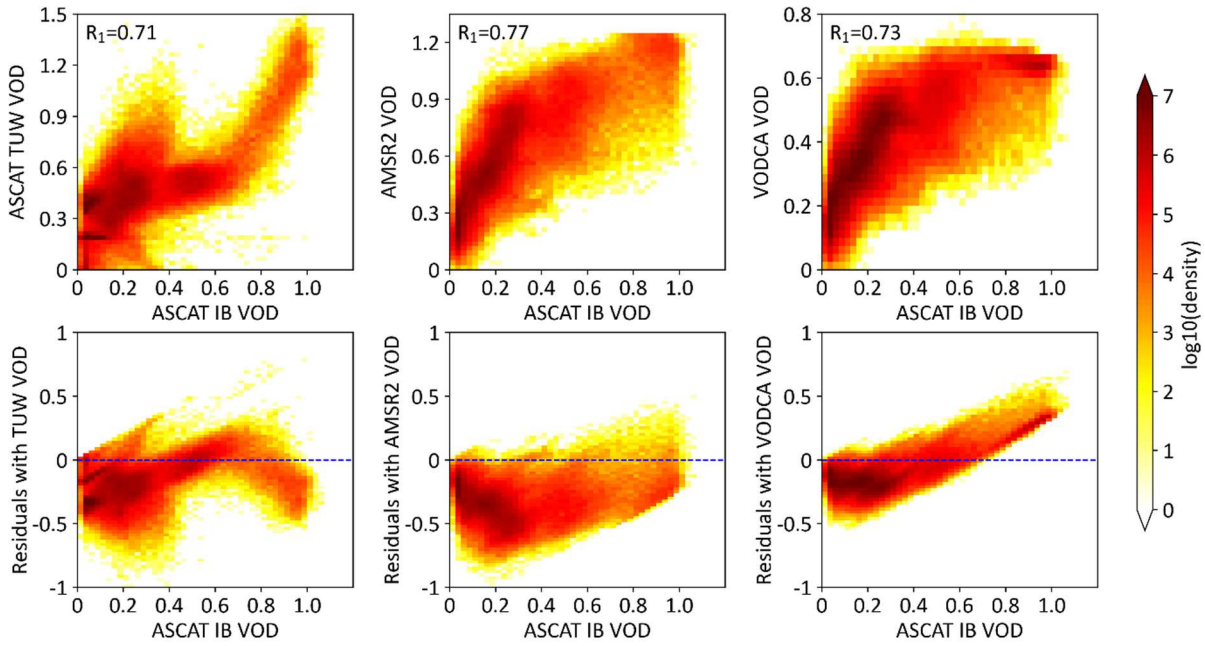

Fig. 8. Density scatter plots and residuals of the spatial relationship between ASCAT VOD IB and the three other VOD products. VOD is time-averaged over 2013-2018, with residuals calculated as ASCAT IB VOD minus the three other VODs.

4.3.2 Spatial correlation with aboveground biomass and canopy height

Fig. 9 shows the density scatter plots of the four VODs with the three aboveground biomass (AGB) products. The density of points in the scatter plots of GEDI AGB is lower than that of the two other AGB products because the range of GEDI biomass did not include areas with latitudes above 53.99°N. The distribution density plot of VOD versus AGB differs between

539 the ASCAT and AMSR2 VOD products. The shape of the density distribution of ASCAT
540 VOD shows a gradual slope rise, while that of AMSR2 VOD presents first a slow slope
541 increase and then a steep increase for AGB greater than ~100 Mg ha^{-1}. Therefore, two
542 different parameterization functions (Eq. (8) for ASCAT VOD; Eq. (9) for AMSR2 VOD)
543 were used to fit the relationship between VOD and AGB. The results show that ASCAT IB
544 VOD exhibits the best performance to predict all three AGB products, with a correlation of
545 0.83-0.87 and RMSE values (34.62-36.86 Mg ha^{-1}) computed between reference and
546 predicted AGB. AMSR2 VOD achieved the second-best performance in predicting the
547 Saatchi and GEDI AGB. Similarly, ASCAT TUW VOD achieved the second-best
548 performance in predicting CCI AGB. ASCAT TUW with Saatchi and GEDI AGB and
549 VODCA with CCI AGB presented the lowest correlation values (0.63-0.66). Note that there
550 is some scatter in these relationships and at low height levels, it cannot be concluded that the
551 C-band VOD product will be a good proxy of the vegetation biomass. In particular, further
552 studies based on specific data sets will be necessary to better evaluate the potential
553 capabilities of ASCAT IB VOD in low vegetation canopies as croplands and grasslands.

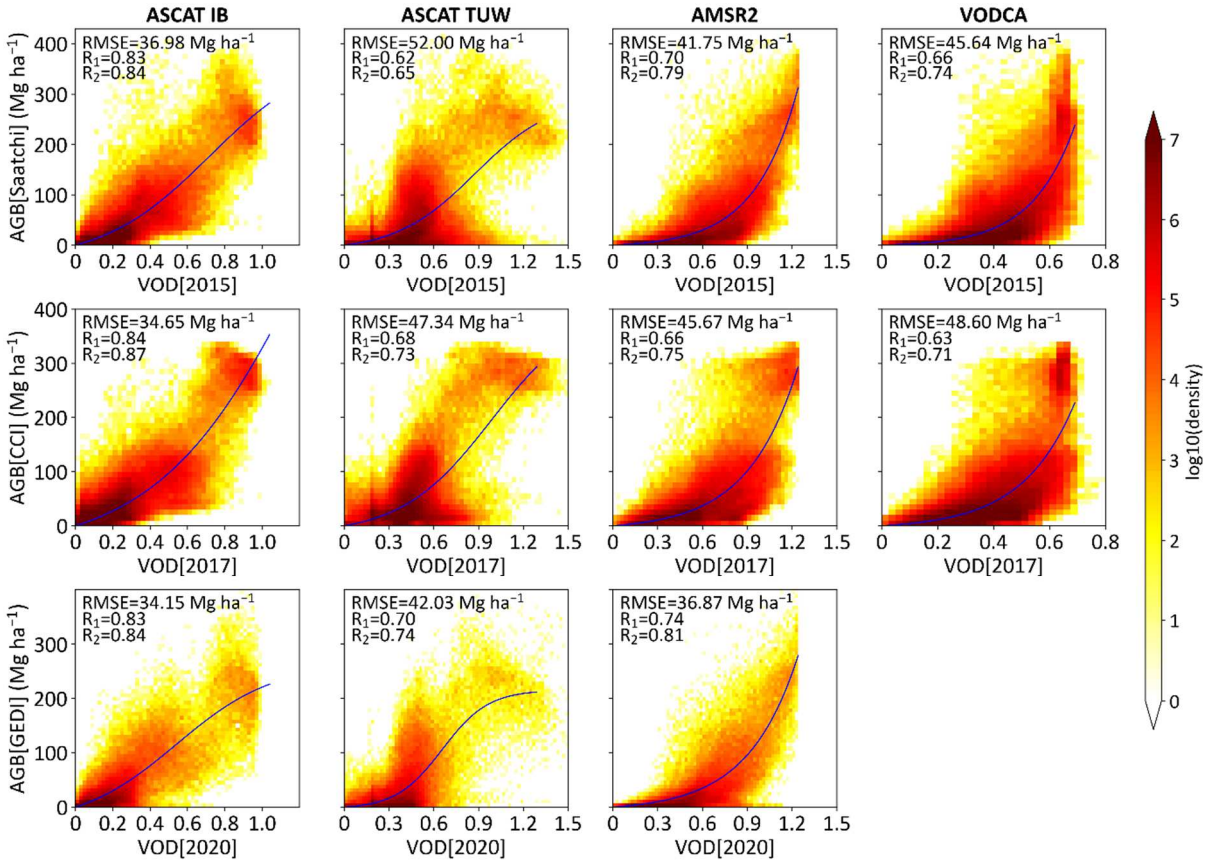

Fig. 9. Density scatter plots of the four global C-VOD (yearly averaged value) *vs* Saatchi AGB (first row), CCI AGB (second row) and GEDI AGB (third row) datasets. R_1 is the spatial Pearson correlation coefficient calculated between C-VOD and AGB (Eq. (7)), while R_2 is calculated between VOD-predicted AGB and AGB. The solid blue lines are the predictive fits obtained using Eqs. (8) or (9).

Considering the density scatter plot (Fig. 10) between VOD and the two GEDI canopy height (CH) (Lang and Potapov) products, ASCAT IB VOD obtained the best correlation (R = 0.84-0.85). The saturation of VOD to CH is more serious for AMSR2 and VODCA VOD than for ASCAT IB and TUW VOD. AMSR2 and VODCA VOD saturate at a value of CH exceeding 15 m, while ASCAT IB and TUW VOD saturate at a higher value (> 20 m). Regarding the potential to predict canopy height, ASCAT IB VOD presents again the best results with the two canopy height (CH) products at different spatial resolutions (Potapov: from 30 m resampled to 0.25 degrees, Lang: 0.5 degrees). The lowest RMSE values were obtained in the

ASCAT IB VOD predictions of CH: RMSE = 4.07 m for Potapov's CH and RMSE = 4.38 m for Lang's CH. The R_2 value (computed using a predictive fit) is lower than the R_1 value for the ASCAT IB VOD. This is mainly because we forced the predictive fitted line to start from (0, 0). The quality of the relationship between VOD and CH is slightly weaker for the Lang product (Fig. 10) probably due to the coarse resolution of the latter product.

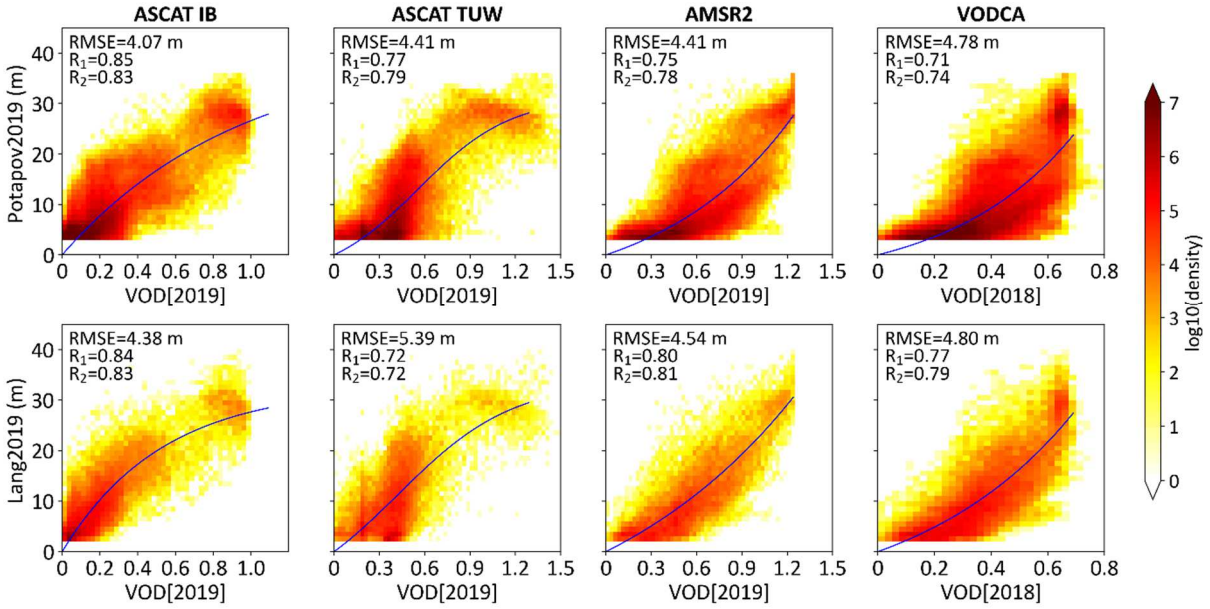

Fig. 10. Density scatter plots of the four global C-VOD (yearly value) *vs* the Potapov et al. canopy height (first row), and Lang et al. canopy height (second row) datasets. R_1 is the spatial Pearson correlation coefficient calculated between C-VOD and canopy height (CH) (Eq. (7)), while R_2 is calculated between VOD-predicted CH and CH. The solid blue lines are the fits obtained using Eq. (8) or (9).

4.3.3 Temporal correlation with vegetation indices

The regions where the four VODs products presented the highest absolute temporal correlation with VIs are shown in Fig. 11. The two ASCAT VODs had more pixels with a higher correlation with LAI and NDWI, with ASCAT IB VOD showing the highest percentage. Passive VODs have a higher correlation with NDVI over more pixels, with AMSR2 VOD having the highest percentage. Similar features can be seen in Fig. 11 (a)-(c)

for the three vegetation indices, with ASCAT IB VOD obtaining the highest correlation values over more pixels in the subtropics regions, same for TUW VOD in the eastern United States, and same for the two AMSR2 VODs in Europe and Australia. The main differences were found in Alaska and central and eastern Russia where ASCAT IB VOD vs. LAI (Fig. 11 (a)) and TUW VOD vs. NDWI (Fig. 11 (c)) showed the highest correlation values, while the two AMSR2 VODs showed highest correlation values with NDVI (Fig. 11 (b)). In central Russia, the two AMSR2 VODs (Fig. 11 (b)-(c)) achieved the highest correlation values with NDWI and NDVI, while the two ASCAT VODs showed the highest correlation values with LAI (Fig. 11 (a)). The pixel-wise temporal correlations between the four VODs and the three VIs are shown in Fig S2. Overall, AMSR2 VODs obtained significant correlations with VIs in more pixels than ASCAT VODs. Specifically, more significant correlations were obtained (i) between AMSR2 VODs and NDVI, and (ii) between ASCAT VODs and LAI. Both the ASCAT VOD and AMSR2 VOD have the lowest number of values significantly associated with NDWI. The spatial distribution of correlation values between the two AMSR2 VODs and the three different VIs is very similar, but the results for the active VODs are significantly different. The correlation values between the two active VODs and the VIs are in opposite directions in some specific regions. In the Amazon and Congo forest regions, ASCAT IB VOD shows negative correlations with the three different VIs, while ASCAT TUW VOD shows positive correlations. In the Central African Republic, northern Argentina and southern Bolivia, ASCAT IB VOD correlates positively with the three different VIs, while ASCAT TUW VOD correlates negatively with the same VIs. For further details, see Fig. S2

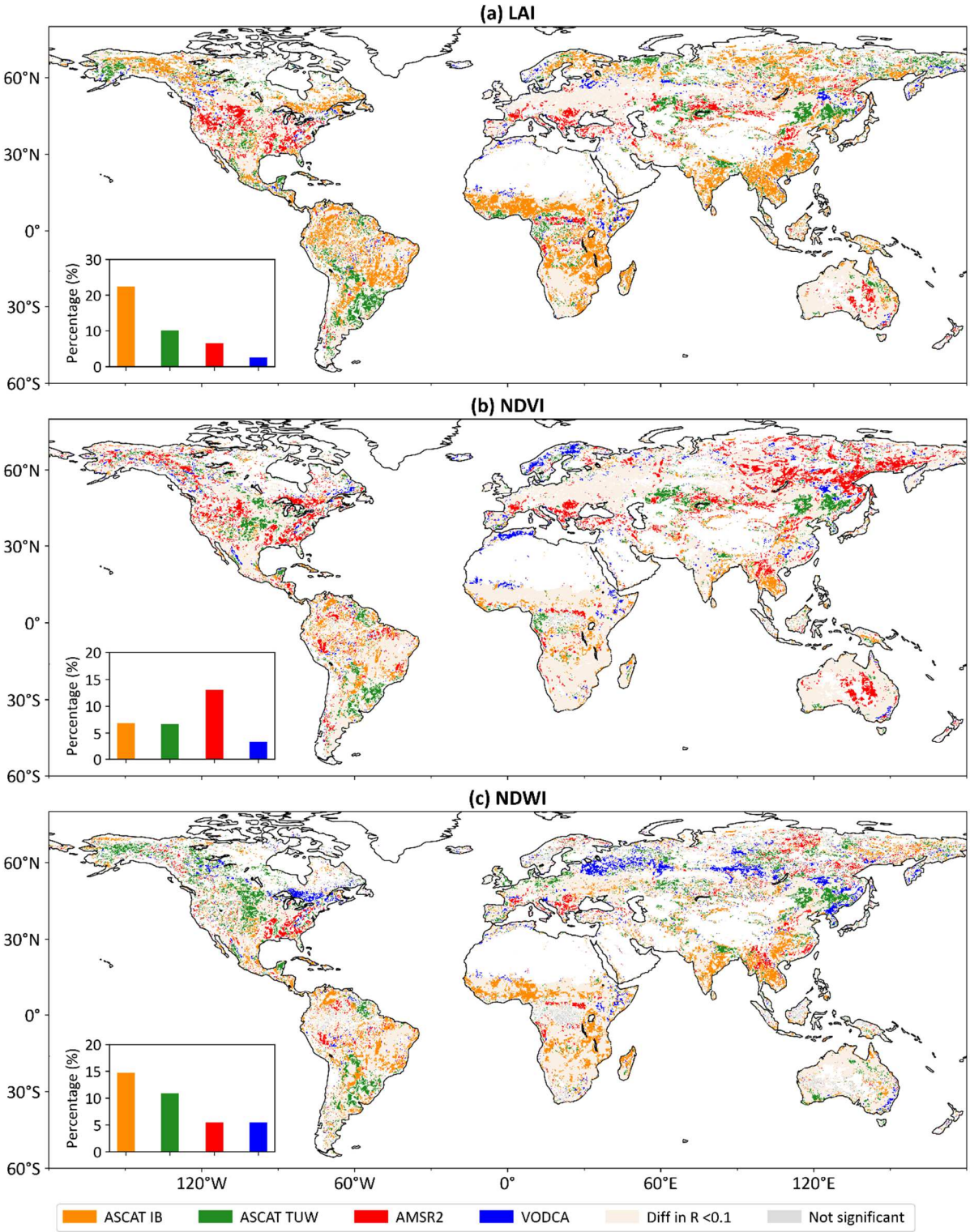

Fig. 11. Maps of the highest absolute temporal correlation (R) values between four VOD datasets and three VIs based on six-year datasets (2013-2018) and corresponding percentage of coverage (bottom left). "Not significant," represented by shaded areas, means the P-value of the correlation is larger than 0.05. White areas mean "no valid data."

To illustrate the seasonal dynamics of the active and passive VODs, the time series of VOD and NDVI (LAI) are plotted over five pixels with relatively homogeneous land cover conditions but different vegetation types (Fig. 12). The fractional coverage of the land cover class and location information of each pixel is presented in Table S4. In the cropland site over northern France, ASCAT IB VOD showed a negative correlation with NDVI and LAI, while the three other VOD products showed the same seasonal dynamics as NDVI and LAI (the ASCAT IB VOD changes were similar to the three other VODs and VIs only from May to July). Fig. 12 (a) illustrates the negative temporal correlations obtained by ASCAT IB VOD with all three VIs in Eastern Europe (Fig. S2). The soil moisture and backscattering coefficient data for both periods (Feb.-May and Aug.-Nov.) were checked (Fig. S3). The backscattering coefficient changes are in phase with the time changes in soil moisture. However, the backscattering coefficient has a high value at the beginning of the vegetation development and the end of senescence, even larger than the value at the time when the LAI was at its peak. Shan et al. (2022) have also identified the same phenomenon that they attributed to human activity before and after sowing and to vegetation senescence in agricultural fields that increased soil roughness resulting in the high value of the observed backscatter signals. In addition, previous studies have observed a decrease in the backscatter signals as LAI increased in narrow-leaved crops (Fontanelli et al., 2013; Macelloni et al., 2001).

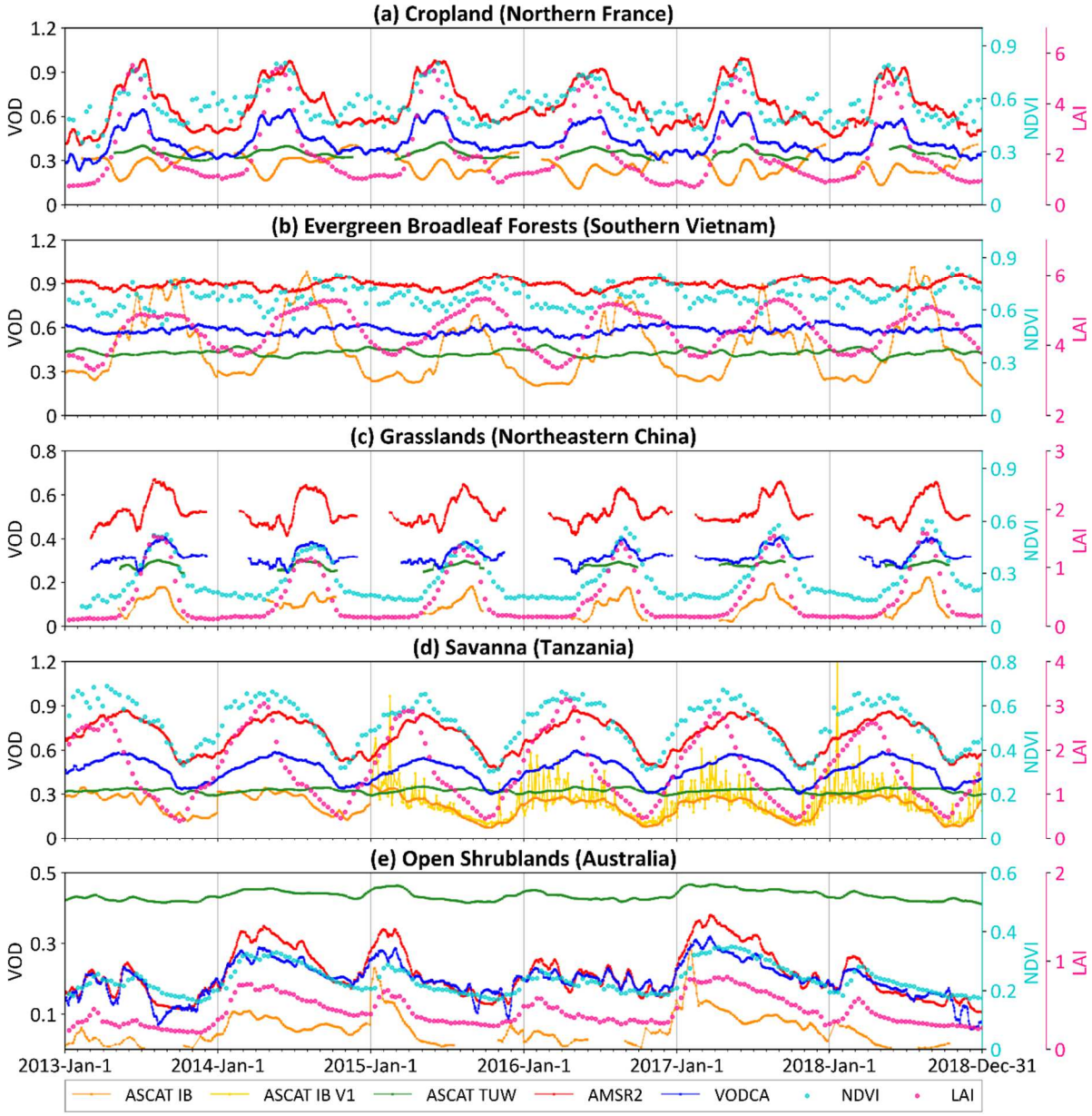

Fig. 12. Time series of the five VOD products (including the old ASCAT IB V1 version in (d)), NDVI, and LAI over five types of vegetation cover in the period from January 2013 to December 2018 (AMSR2 and VODCA VOD were smoothed by an 18-day moving window).

Interestingly, over the evergreen broadleaf forest site in southern Vietnam, ASCAT IB VOD presents large seasonal variations similar to those of LAI, while the three other VODs and NDVI showed slight time variations. In the high latitude grasslands site (Fig. 12 (c)), the temporal availability of ASCAT IB VOD is shorter than that of the passive VODs, but ASCAT IB VOD still monitored well the vegetation growth. The AMSR2 VODs have a

longer temporal availability than the active VODs in the high latitude regions, which is clearly shown in the Hovmöller diagrams (Fig. S4). In the savanna site in Africa (Fig. 12 (d)), the peak of ASCAT IB VOD is well synchronized with that of LAI, while the AMSR2 VODs and NDVI are more synchronized. Compared to the ASCAT IB V1 VOD version (only available in Africa) (Liu et al., 2021b), it can be clearly seen that the new global ASCAT IB VOD product is smoother and solves the noise issue mentioned in the previous study in Africa. In the open shrublands site (Fig. 12 (e)), the values of LAI and NDVI were higher in 2017 than in the other three years, and ASCAT IB VOD also captured well this inter-annual variation in the vegetation cycle. ASCAT TUW VOD presents weak temporal variations over all the different vegetation types, because a time window ranging from 2 to 12 weeks were used to calculate VOD (Vreugdenhil et al., 2016).

5. Discussion

5.1 Uncertainty in the VOD retrieval

There are three main uncertainties associated with ASCAT IB VOD. The first one is the simplified scattering process considered in the retrieval algorithms, and the other two are the soil parameters estimated from the random forest models and the ERA5-Land SM input. The water cloud model that is used to simulate the backscattering coefficient in the present study neglected the multiple scattering effects as it is hard to quantify this part in the model. Some studies showed that the multiple scattering effects can be generally ignored for low levels of the vegetation cover at the C- and L-bands (El Hajj et al., 2019b; Hosseini et al., 2015; Zribi et al., 2019). One study (Li et al., 2020) confirmed also this conclusion by comparing the VOD and SM parameters retrieved from L-band SMOS TB based on Tau-Omega and a higher order radiative transfer model, named the Two-Stream emission model (Schwank et al., 2018), which holds a stronger physical background with consideration of multiple scattering and reflection. However, the VOD values retrieved from the two models vary over

dense vegetation areas and boreal regions. A study that explored the contribution of double-bounce to the total signal of the P-, L- and C-bands in forest regions showed that the double-bounce component at C-band is lower than that at the L- and P-bands and accounts for a small contribution (1%) to the total signal in forests (Freeman and Durden, 1993). Quast et al. (2019) used a generalization of the WCM that incorporates an estimate of first-order (i.e., double-bounce) interaction-effects to simulate the ASCAT backscattering signals. The results also showed the interaction-contributions are very small. In the passive domain, (it is likely it is the same in the active domain), several studies showed that multiple scattering effects can be well accounted for by zero-order radiative transfer models that neglect multiple scattering effects, provided that the model parameters (VOD and scattering parameter) are considered as effective parameters (Kurum, 2013; Li et al., 2020). Here, we roughly simulated the effect of neglecting multiple scattering, by accounting for the impact of a 0 to 5 % change in the total signal (the value of 0 to 5 % was estimated from Freeman and Durden (1993) and Quast et al. (2019)), on VOD retrievals for the three vegetation types (Fig. S5). Assuming multiple scattering accounts for 5 % of the total signal (worst-case scenario), the results showed that the relative variation of VOD in the evergreen broadleaf forest reached 19 % when ignoring multiple scattering. The relative change of VOD in grasslands also showed a higher value (17 %) than in savannah (12 %) even though their VOD value changed little (~ 0.02). These results show that neglecting multiple scattering effects in ASCAT VOD retrievals has a non-negligible effect, potentially leading to a change in VOD values by around 10-20 % in the worst case and that better consideration of multiple scattering effects should be considered in future improvements to our retrieval approach. However, the relative change in VOD caused by neglecting multiple scattering is relatively small compared to the large uncertainties associated with global AGB datasets: AGB values can vary by up to 50 % in some forest regions for different AGB data sets (Araza et al., 2022; Urbazaev et al., 2018). Considering

689 that there is no simple equation to quantitatively describe the multiple scattering effects in
690 WCM, the traditional WCM equations were used in this study. Although there are some
691 discrete models (Bracaglia et al., 1995; Ulaby et al., 1990) that considered the multiple
692 scattering effects, it is difficult to apply these models over large regions as they need too
693 many input parameters for a rigorous retrieval (Bai et al., 2018; Bai et al., 2022).

694 Another possible uncertainty associated with ASCAT IB VOD is related to the fact we
695 ignored the subsurface scattering in the simplified Ulaby soil model. Wagner et al. (2022)
696 showed that the backscattering coefficient negatively correlates with SM when subsurface
697 scattering is the main contribution of the soil backscatter and positively correlates with SM
698 when the surface scattering effects dominate. When both types of scattering are present, the
699 backscattering coefficient will exhibit a negative correlation with SM in dry conditions and a
700 positive correlation as SM gradually increases, showing a U-shape (Liu et al., 2016; Wagner
701 et al., 2022). Based on the correlation with AGB, the ASCAT IB VOD retrieved using the soil
702 parameters predicted by different models trained with different positive correlation thresholds
703 were evaluated, with the threshold $R > 0.25$ achieving the best results (Table S5). When a
704 higher threshold value is selected, pixels with mixed scattering that may be U-shaped with a
705 lower R-value are excluded from the model training, resulting in more errors in the soil
706 parameters prediction and finally causing errors in the ASCAT IB VOD retrieval. Although
707 some studies have showed that the subsurface scattering effects usually happen in dry desert
708 areas (McColl et al., 2014), the correlation values between the ASCAT backscatter
709 measurements and ERA5-land SM revealed that pixels with negative correlation values are
710 also located in some sparsely vegetated areas (Fig. 1 in (Wagner et al., 2022)). Because of the
711 negative correlation, the σ°_{WetRef} parameter fails to represent the time period when SM values
712 are high (Fig. S1). Therefore, neglecting subsurface scattering in soil scattering modeling and
713 in estimating initial values of the vegetation parameter from σ°_{WetRef} will introduce

uncertainty to the ASCAT IB VOD retrievals, especially when the subsurface effects are dominant.

Random forest models were used in this study to simulate the global *C* and *D* soil model parameters. The underestimation of the high values and overestimation of the low values of the soil parameters (*C* and *D*) can be noted in the 10-fold cross-validation (Fig. 4 (a)-(b)). This is caused by the limitations of the tree-based (e.g. random forest) models to perform extrapolations (Hengl et al., 2018). The predictions for test data outside the range of training data are often underestimated or overestimated. During the 10-fold cross-validation, the data are divided into ten groups with 9 groups used for training and 1 group for testing, and each group is tested once for the model. The range of data in the training and testing folds may be similar if the data has a normal distribution, where the mean is equal to the median value. In the histogram of the *C* and *D* values extracted in "bare soil" pixels (Fig. S6), there is a larger difference between the averaged and median value of the *D* values than for the *C* values. As a result, the underestimation and overestimation of the *D* model are more severe than that of the *C* model (Fig. 4 (a)-(b)). The effect of the uncertainty associated with the parameters *C* and *D* on the VOD retrievals was evaluated on three vegetation types based on RMSE in Fig. 4. The results (Fig. S7) show that the most significant impact is on grasslands, followed by savannas and evergreen broadleaf forests. Following the method of Liu et al. (2021b), the uncertainty associated with ERA5-Land's SM on the VOD retrievals was analyzed by examining changes in SM values in relation to relative changes in VOD values over three vegetation types. The selected change in SM value, derived from an estimate of ERA5-Land's ubRMSE, is 0.05 m^3/m^3. The results (Fig. S8) show that the relative change in VOD values is ± 17 % on grassland, ± 8 % on savannah and ± 3 % on evergreen broadleaf forest when SM values vary by ± 0.05 m^3/m^3. As expected, the impact of errors on SM is weaker as VOD values increase.

These results are similar to the sensitivity analysis of the uncertainty associated with ERA5-Land SM on ASCAT IB V1 VOD retrievals (Liu et al., 2021b).

5.2 Inter-comparison of the active and passive VOD

The assessment and comparison results indicate that there are some discrepancies between ASCAT IB VOD and AMSR2 VODs. Regarding spatial relationships, ASCAT IB VOD showed the highest correlation with AGB and canopy height (Fig. 9-10). It was also found that ASCAT IB VOD had the best temporal correlation with LAI and NDWI for most of the pixels at the global scale, while AMSR2 VODs showed best correlation with NDVI (Fig. 11 (b)). The statistics of the temporal correlation between VODs and VIs in each land cover type show similar results (Table S6), especially for short vegetation. Physical radiative transfer mechanisms may help to understand why LAI and NDWI have a better spatial and temporal correlation with active ASCAT IB VOD than passive AMSR2 VODs. As active microwave sensors emit energy, the observed backscattering coefficient is a measurement of the microwave radiation scattered in a single backward direction, while the passive microwaves sensors detect the naturally emitted microwave energy which corresponds to the integration of the bi-static coefficient considering the incident radiations over the whole hemisphere (Ferrazzoli et al., 1989; Wigneron et al., 1999). Therefore, compared to passive observations, active observations are more sensitive to volume scattering within the canopy. This is because passive microwave remote sensing integrates over all of the possible directions of incident radiation, while active microwave remote sensing only samples a single direction, resulting in less averaging of coherent effects. Consequently, active microwave remote sensing is more sensitive to vegetation canopy structure and specifically temporal changes in leaf water and orientation than passive microwave remote sensing.

Even though ASCAT IB VOD performed well in space and time when compared with the three other C-band VOD products, we should be aware that the algorithms and input datasets

763 of those four products differ and also make the VOD values and ranges different (Fig. 8). We
764 summarized these main differences in Table 1. For the two active VOD products, the retrieval
765 algorithms are both based on the water cloud model, but the inputs are different. TUW VOD
766 was retrieved by using the ASCAT dry and wet references which are the mean value of the 10%
767 highest and lowest normalized backscatter data at 25° and 40° (Pfeil et al., 2018), while the
768 ASCAT normalized backscatter data at 40° was used to retrieve ASCAT IB VOD. The
769 hypotheses made in the two active VOD retrieval algorithms are also very different. In the
770 ASCAT IB VOD retrieval algorithm, the vegetation scattering (ω) and VOD parameters were
771 assumed to be constant within a period of 18 days and retrieved together using a model-based
772 SM as input to the algorithm. In contrast, the TUW VOD retrieval algorithm assumes that the
773 maximum range of backscatter values (- 6.68 dB) over bare soil is the same around the world,
774 excluding desert areas. The auxiliary data used by both algorithms mainly concern the
775 modelling of soil scattering. The ASCAT IB VOD retrieval algorithm employed many
776 ancillary data sets (*e.g.* SoilGrids250m and DEM-related datasets) for calibrating the
777 parameters of the soil model and used a modelled reanalysis SM product from ERA5-land as
778 input to the soil model. Conversely, the TUW VOD retrieval algorithm utilized only the
779 Koppen–Geiger climate classification data to model the bare soil scattering. The different
780 ancillary data used in the two algorithms will affect the VOD retrievals. The most obvious
781 difference is that the two active VODs are retrieved using ancillary information for soil
782 moisture, while VOD and SM are simultaneously retrieved in the passive domain (Owe et al.,
783 2008; Wigneron et al., 2017). The two passive VOD are retrieved from AMSR2 brightness
784 temperature measurements at 55° (Imaoka et al., 2012) but with different versions of the
785 LPRM algorithm. VODCA VOD was retrieved based on LPRM version 6 (van der Schalie et
786 al., 2017) which update the setting of the effective scattering albedo and of the soil roughness
787 parameter, compared with LPRM version 5 used in the AMSR2 VOD retrievals. Those

788 discrepancies among the four VOD products may make the interpretation of the inter-
789 comparison more challenging.

790 **Table 1.** Summary of the key differences in the retrieval algorithms of the active ASCAT
791 VODs (ASCAT IB, TUW) and the passive VODs (AMSR2 and VODCA).

Algorithm	ASCAT IB	ASCAT TUW (Vreugdenhil et al., 2016)	LPRM version 5 (AMSR2 VOD) (Owe et al., 2008)	LPRM version 6 (VODCA VOD) (Moesinger et al., 2020 ; van der Schalie et al., 2017)
Observations	ASCAT σ°_{obs} at VV polarization	ASCAT σ°_{WetRef} and σ°_{DryRef} at VV polarization	AMSR2 T_B at dual (V, H) polarization	AMSR2 at dual (V, H) polarization
Vegetation scattering modelling	Water cloud model (Attema and Ulaby, 1978)	Water cloud model (Attema and Ulaby, 1978)	τ-ω_p model (Mo et al., 1982) ω_p= 0.05	τ-ω_p model (Mo et al., 1982) ω_p= 0.075
Soil scattering modelling	Ulaby linear model (Ulaby et al., 1978)	$\Delta\sigma^{\circ}_{S}$: maximum range in backscatter values over bare soils	H-Q-N modelling (Wang and Choudhury, 1981) H_R= 0.09	H-Q-N modelling (Wang and Choudhury, 1981) H_R= 1.2*(1-2*SM)
Hypothesis	VOD is the same over a short time window (18 days)	$\Delta\sigma^{\circ}_{S}$ is the same everywhere in the world, except in desert areas.	VOD is the same at H and V polarizations	VOD is the same at H and V polarizations
Ancillary data	SoilGrids250m (Hengl et al., 2017) and DEM-related data (Danielson and Gesch, 2011) are used to estimate the soil parameters of the Ulbay linear model; ERA5-Land SM (Muñoz-Sabater et al., 2021) is used as input to simulate the bare soil backscatter coefficient	Koppen–Geiger climate classification was used to set the $\Delta\sigma^{\circ}_{S}$ parameter	Vertically polarized Ka-band (36.5 GHz) observations from AMSR2 are used to derive the effective temperature (Holmes et al., 2009); Soil texture (clay, silt and sand) from FAO is used to estimate the soil dielectric constant (Wang and Choudhury, 1981)	Same with LPRM version 5
VOD retrieval	VOD is retrieved simultaneously with the vegetation scattering parameter (ω)	Only VOD is retrieved	VOD is retrieved simultaneously with SM	VOD is retrieved simultaneously with SM, VOD is re-scaled to AMSR-E VOD by a CDF matching technique

Limitations	The multi-temporal method may result in VOD not being sensitive to dry-down periods (Li et al., 2021) and has larger uncertainties over grasslands and croplands where vegetation growth can be very fast (Jackson et al., 2004).	The use of a kernel smoother with a half-width window of 21 days (Vreugdenhil et al., 2020) when calculating σ°_{WetRef} and σ°_{DryRef} decrease the seasonal amplitude of VOD; σ°_{WetRef} and σ°_{DryRef} are not optimized for regional conditions (Pfeil et al., 2018) .	The global constant value of ω_p and H_R may cause uncertainties in VOD retrieval (Baur et al., 2019).	Same with LPRM version 5

T_B = brightness temperature; ω_p = Effective scattering albedo; H_R = roughness parameter

6. Conclusion and Outlook

The objective of this work was to retrieve the first global ASCAT IB VOD product and the vegetation scattering parameter (ω) from the single-channel (VV) active microwave observations of ASCAT. The spatial distribution of the retrieved ω map matches well vegetation distribution, which is in line with the previous findings of the literature. When compared to the other C-VOD products, ASCAT IB VOD had a competitive advantage. In spatial terms, ASCAT IB VOD presented the highest correlation values with AGB and tree height, with R values of ~0.83 and ~ 0.84, respectively. In comparison with the previous ASCAT IB V1 VOD developed only over Africa, the global ASCAT IB VOD has shown strong improvement in terms of temporal evolution which are much less noisy pixel-based time-series than those of the previous version. Some interesting discrepancies were also observed between ASCAT and AMSR2 VODs. The non-linear density distribution presented by ASCAT VOD and AGBs is different from that presented by AMSR2 VOD. ASCAT VODs have a linear spatial relationship with LAI and a non-linear one with NDWI and NDVI, while AMSR2 VODs presented opposite results (Fig. S9). Similar results were obtained in terms of temporal variations: ASCAT VODs show greater synchronization with LAI and NDWI, while AMSR2 VODs are more closely aligned with NDVI. So, the different characteristics of the two ASCAT VODs (more closely related to changes in LAI) and the two AMSR2 VODs (more closely related to changes in NDVI and NDWI) showed appealing complementarity for conducting joint vegetation studies.

The strong ability of ASCAT observations to predict AGB as found in this work and Santoro et al. (2022) encourages us to apply this long-term VOD to investigate the time changes in aboveground biomass at continental scales since 2007. Recently, Tao et al. (2022) developed the first global C-band scatterometer dataset which dates back to 1992. Applying the new ASCAT IB algorithm to this dataset would allow obtaining a 30-year data set of the VOD parameter which is very promising for studies of vegetation resilience (Forzieri et al., 2022). Considering that global ASCAT IB VOD showed a good sensitivity to NDWI, some applications (like wildfire prediction or post-fire recovery) related to vegetation water content can be explored in the future (Bousquet et al., 2022; Fan et al., 2018). Furthermore, a specific version of our algorithm could be developed for Sentinel-1 (S1): less uncertainty in the retrievals could be obtained by combining the S1 observations at the two VV and VH polarisations, instead of using only one (VV) for ASCAT. In addition, improved bare soil models and the use of machine learning methods that can be extrapolated (e.g. ensemble RF, Cubist) (Lin et al., 2017; Pouladi et al., 2019) could lead to a decrease in the uncertainty associated with the simulation of the bare soil backscattering.

Data availability

Global ASCAT IB VOD and vegetation scattering parameter (ω) can be downloaded from the INRAE Bordeaux remote sensing lab website (https://ib.remote-sensing.inrae.fr) after registration.

Appendix A

A.1 Random forest model

In this study, the random forest (RF) regression model was used to simulate the global soil parameters (*C* and *D*) of the Ulaby bare soil model. RF is a tree-based machine learning

method and has been widely adopted in many geographic-related studies (Liao et al., 2022; Wang et al., 2022). RF works by training many regression trees and reporting the mean response over all the trees. In each tree, approximately two-thirds of the samples in the dataset are used for training and the remaining third (called the out-of-bag data (OOB)) are used for internal validation of the model. The r-square values (R^2) and RMSE calculated from the OOB samples are used to assess the model performance. The python sklearn package (Pedregosa et al., 2011) was used for the implementation of RF, including the establishment of the model, the selection of the predictor of the model, and the validation of the model.

The '*RandomForestRegressor*' was used as the estimator and its two parameters (n_estimators and max_features) were optimized by the '*GridSearchCV*' function. The 'random_state' has been defined to guarantee the reproducibility of the model. The predictor variables of the model were selected using a recursive feature elimination (RFE) method (Guyon et al., 2002). We first fitted the model with all the predictors and then removed the least important predictor from the model. This process was iterated until only one predictor variable was left. The selected predictors are those that lead to the highest R^2 and lowest RMSE. Finally, the 10-fold cross-validation (CV) (Stone, 1974) was used as an independent validation to assess the accuracy of the selected model. The mean value of the R^2 and RMSE of 10-fold CV and the importance of each predictor were reported.

Appendix Table 1

Statistics of *C* and *D* at the global scale.

Parameter	Max	95th percentiles	Min	5th percentiles	Mean	Median
C(dB)	-7.60	-11.82	-26.01	-18.05	-14.27	-13.92
D (dB/ $m^3 \cdot m^{-3}$)	34.12	13.97	1.75	5.12	8.46	9.76

Appendix Table 2

Statistics of *C* and *D* over different ranges of values.

Parameter	Range [Min, Max]	Percentage	Mean	Median
C (dB)	[-25,-20]	1.51 %	-21.05	-20.78

	[-20,-15]	21.98 %	-16.64	-16.38
	[-15,-12.5]	66.62 %	-13.73	-13.72
	[-12.5,-10]	9.58 %	-11.65	-11.85
	[-10,-5]	0.31 %	-9.53	-9.70
D ($dB/ m^3 \cdot m^{-3}$)	[0,5]	3.96 %	4.57	4.67
	[5,7.5]	38.79 %	6.38	6.43
	[7.5,10]	36.47 %	8.63	8.59
	[10,15]	17.31 %	11.74	11.47
	[15,25]	3.39 %	17.67	16.95
	[25,35]	0.08 %	26.92	26.32

Appendix Table 3

Statistics of *C* and *D* for different IGBP land cover classes.

IGBP land cover	Min		Max		Mean		Median		Percentage
	C	D	C	D	C	D	C	D	
ENF	-16.48	3.88	-9.83	12.88	-13.12	7.12	-13.34	6.83	2.17 %
EBF	-16.81	4.52	-9.79	16.14	-14.02	8.86	-14.21	8.84	7.32 %
DBF	-17.28	4.10	-10.09	18.00	-13.80	8.59	-13.90	8.51	1.80 %
DNF	-15.34	5.42	-12.35	12.42	-13.90	9.11	-13.92	8.86	0.11 %
MFO	-16.53	3.83	-9.91	16.82	-13.42	8.82	-13.43	8.34	4.84 %
CSH	-17.39	4.08	-10.76	13.19	-14.51	7.22	-14.55	6.64	0.23 %
OSH	-21.04	1.75	-9.17	30.59	-13.85	6.76	-13.44	6.38	13.15 %
WSA	-20.09	4.13	-9.90	16.91	-13.69	8.21	-13.69	8.07	10.03 %
SAV	-19.61	3.05	-10.25	17.46	-13.82	8.04	-13.78	7.95	13.44 %
GRA	-26.01	2.06	-8.72	34.12	-14.43	9.02	-14.01	8.00	23.48 %
CRO	-22.01	2.81	-1.08	26.35	-14.67	10.88	-14.53	10.86	9.64 %
CVM	-18.40	4.63	-12.31	22.20	-14.34	9.84	-14.17	9.65	0.61 %
BSV	-20.43	2.23	-7.60	24.42	-15.76	7.81	-15.99	7.31	13.18 %

References

Al Bitar, A., Mialon, A., Kerr, Y.H., Cabot, F., Richaume, P., Jacquette, E., Quesney, A., Mahmoodi, A., Tarot, S., Parrens, M., Al-Yaari, A., Pellarin, T., Rodriguez-Fernandez, N., & Wigneron, J.-P. (2017). The global SMOS Level 3 daily soil moisture and brightness temperature maps. *Earth System Science Data, 9*, 293-315

Araza, A., de Bruin, S., Herold, M., Quegan, S., Labriere, N., Rodriguez-Veiga, P., Avitabile, V., Santoro, M., Mitchard, E.T.A., Ryan, C.M., Phillips, O.L., Willcock, S., Verbeeck, H., Carreiras, J., Hein, L., Schelhaas, M.-J., Pacheco-Pascagaza, A.M., da Conceição Bispo, P., Laurin, G.V., Vieilledent, G., Slik, F., Wijaya, A., Lewis, S.L., Morel, A., Liang, J., Sukhdeo, H., Schepaschenko, D., Cavlovic, J., Gilani, H., & Lucas, R. (2022). A comprehensive framework for assessing the accuracy and uncertainty of global above-ground biomass maps. *Remote Sensing of Environment, 272*

Asner, G.P., Clark, J.K., Mascaro, J., Galindo García, G.A., Chadwick, K.D., Navarrete Encinales, D.A., Paez-Acosta, G., Cabrera Montenegro, E., Kennedy-Bowdoin, T., Duque, Á., Balaji, A., von Hildebrand, P., Maatoug, L., Phillips Bernal, J.F., Yepes Quintero, A.P., Knapp, D.E., García Dávila, M.C., Jacobson, J., & Ordóñez, M.F. (2012). High-resolution mapping of forest carbon stocks in the Colombian Amazon. *Biogeosciences, 9*, 2683-2696

Attema, E.P.W., & Ulaby, F.T. (1978). Vegetation modeled as a water cloud. *Radio Science, 13*, 357-364

876 Baghdadi, N., Cerdan, O., Zribi, M., Auzet, V., Darboux, F., El Hajj, M., & Kheir, R.B. (2008). Operational
877 performance of current synthetic aperture radar sensors in mapping soil surface characteristics in agricultural
878 environments: application to hydrological and erosion modelling. *Hydrological Processes, 22*, 9-20

879 Baghdadi, N.N., El Hajj, M., Zribi, M., & Fayad, I. (2016). Coupling SAR C-Band and Optical Data for Soil
880 Moisture and Leaf Area Index Retrieval Over Irrigated Grasslands. *IEEE Journal of Selected Topics in Applied*
881 *Earth Observations and Remote Sensing, 9*, 1229-1243

882 Bai, X., Zeng, J., Chen, K.-S., Li, Z., Zeng, Y., Wen, J., Wang, X., Dong, X., & Su, Z. (2018). Parameter
883 Optimization of a Discrete Scattering Model by Integration of Global Sensitivity Analysis Using SMAP Active
884 and Passive Observations. *IEEE Transactions on Geoscience and Remote Sensing*, 1-16

885 Bai, X., Zheng, D., Liu, X., Fan, L., Zeng, J., & Li, X. (2022). Simulation of Sentinel-1A observations and
886 constraint of water cloud model at the regional scale using a discrete scattering model. *Remote Sensing of*
887 *Environment, 283*

888 Beck, H.E., Pan, M., Miralles, D.G., Reichle, R.H., Dorigo, W.A., Hahn, S., Sheffield, J., Karthikeyan, L.,
889 Balsamo, G., Parinussa, R.M., van Dijk, A.I.J.M., Du, J., Kimball, J.S., Vergopolan, N., & Wood, E.F. (2020).
890 Evaluation of 18 satellite- and model-based soil moisture products using in situ measurements from 826 sensors

891 Boulton, C.A., Lenton, T.M., & Boers, N. (2022). Pronounced loss of Amazon rainforest resilience since the
892 early 2000s. *Nature Climate Change, 12*, 271-278

893 Bousquet, E., Mialon, A., Rodriguez-Fernandez, N., Mermoz, S., & Kerr, Y. (2022). Monitoring post-fire
894 recovery of various vegetation biomes using multi-wavelength satellite remote sensing. *Biogeosciences, 19*,
895 3317-3336

896 Bracaglia, M., Ferrazzoli, P., & Guerriero, L. (1995). A fully polarimetric multiple scattering model for crops.
897 *Remote Sensing of Environment, 54*, 170-179

898 Canisius, F., Shang, J., Liu, J., Huang, X., Ma, B., Jiao, X., Geng, X., Kovacs, J.M., & Walters, D. (2018).
899 Tracking crop phenological development using multi-temporal polarimetric Radarsat-2 data. *Remote Sensing of*
900 *Environment, 210*, 508-518

901 Carreiras, J.M.B., Quegan, S., Le Toan, T., Ho Tong Minh, D., Saatchi, S.S., Carvalhais, N., Reichstein, M., &
902 Scipal, K. (2017). Coverage of high biomass forests by the ESA BIOMASS mission under defense restrictions.
903 *Remote Sensing of Environment, 196*, 154-162

904 Chang, Q., Zwieback, S., DeVries, B., & Berg, A. (2022). Application of L-band SAR for mapping tundra shrub
905 biomass, leaf area index, and rainfall interception. *Remote Sensing of Environment, 268*

906 Chaparro, D., Duveiller, G., Piles, M., Cescatti, A., Vall-llossera, M., Camps, A., & Entekhabi, D. (2019).
907 Sensitivity of L-band vegetation optical depth to carbon stocks in tropical forests: a comparison to higher
908 frequencies and optical indices. *Remote Sensing of Environment, 232*

909 Chen, Y., Feng, X., & Fu, B. (2021). An improved global remote-sensing-based surface soil moisture (RSSSM)
910 dataset covering 2003–2018. *Earth System Science Data, 13*, 1-31

911 Conrad, O., Bechtel, B., Bock, M., Dietrich, H., Fischer, E., Gerlitz, L., Wehberg, J., Wichmann, V., & Böhner,
912 J. (2015). System for Automated Geoscientific Analyses (SAGA) v. 2.1.4. *Geoscientific Model Development, 8*,
913 1991-2007

Danielson, J.J., & Gesch, D.B. (2011). *Global multi-resolution terrain elevation data 2010 (GMTED2010)*. US Department of the Interior, US Geological Survey

Du, J., Kimball, J.S., & Jones, L.A. (2016). Passive Microwave Remote Sensing of Soil Moisture Based on Dynamic Vegetation Scattering Properties for AMSR-E. *IEEE Transactions on Geoscience and Remote Sensing, 54*, 597-608

Dubayah, R.O., Armston, J., Healey, S.P., Yang, Z., Patterson, P.L., Saarela, S., Stahl, G., Duncanson, L., & Kellner, J.R. (2022). GEDI L4B Gridded Aboveground Biomass Density, Version 2. In: ORNL Distributed Active Archive Center

El Hajj, M., Baghdadi, N., Wigneron, J.-P., Zribi, M., Albergel, C., Calvet, J.-C., & Fayad, I. (2019a). First Vegetation Optical Depth Mapping from Sentinel-1 C-band SAR Data over Crop Fields. *Remote Sensing, 11*

El Hajj, M., Baghdadi, N., & Zribi, M. (2019b). Comparative analysis of the accuracy of surface soil moisture estimation from the C- and L-bands. *International Journal of Applied Earth Observation and Geoinformation, 82*

Fan, L., Wigneron, J.-P., Ciais, P., Chave, J., Brandt, M., Sitch, S., Yue, C., Bastos, A., Li, X., Qin, Y., Yuan, W., Schepaschenko, D., Mukhortova, L., Li, X., Liu, X., Wang, M., Frappart, F., Xiao, X., Chen, J., Ma, M., Wen, J., Chen, X., Yang, H., van Wees, D., & Fensholt, R. (2022). Siberian carbon sink reduced by forest disturbances. *Nature Geoscience*

Fan, L., Wigneron, J.P., Ciais, P., Chave, J., Brandt, M., Fensholt, R., Saatchi, S.S., Bastos, A., Al-Yaari, A., Hufkens, K., Qin, Y., Xiao, X., Chen, C., Myneni, R.B., Fernandez-Moran, R., Mialon, A., Rodriguez-Fernandez, N.J., Kerr, Y., Tian, F., & Penuelas, J. (2019). Satellite-observed pantropical carbon dynamics. *Nat Plants, 5*, 944-951

Fan, L., Wigneron, J.P., Xiao, Q., Al-Yaari, A., Wen, J., Martin-StPaul, N., Dupuy, J.L., Pimont, F., Al Bitar, A., Fernandez-Moran, R., & Kerr, Y.H. (2018). Evaluation of microwave remote sensing for monitoring live fuel moisture content in the Mediterranean region. *Remote Sensing of Environment, 205*, 210-223

Fernandez-Moran, R., Wigneron, J.P., De Lannoy, G., Lopez-Baeza, E., Mialon, A., Mahmoodi, A., Parrens, M., Al Bitar, A., Richaume, P., & Kerr, Y. (2016). Calibrating the Effective Scattering Albedo in the Smos Algorithm: Some First Results. *2016 Ieee International Geoscience and Remote Sensing Symposium (Igarss)*, 826-829

Ferrazzoli, P., Luzi, G., Paloscia, S., Pampaloni, P., Schiavon, G., & Solimini, D. (1989). Comarison between the microwave emissivity and backscatter coefficient of crops. *IEEE Transactions on Geoscience and Remote Sensing, 27*, 772-778

Figa-Saldaña, J., Wilson, J.J.W., Attema, E., Gelsthorpe, R., Drinkwater, M.R., & Stoffelen, A. (2014). The advanced scatterometer (ASCAT) on the meteorological operational (MetOp) platform: A follow on for European wind scatterometers. *Canadian Journal of Remote Sensing, 28*, 404-412

Fontanelli, G., Paloscia, S., Zribi, M., & Chahbi, A. (2013). Sensitivity analysis of X-band SAR to wheat and barley leaf area index in the Merguellil Basin. *Remote Sensing Letters, 4*, 1107-1116

Forzieri, G., Dakos, V., McDowell, N.G., Ramdane, A., & Cescatti, A. (2022). Emerging signals of declining forest resilience under climate change. *Nature*

952 Frappart, F., Wigneron, J.-P., Li, X., Liu, X., Al-Yaari, A., Fan, L., Wang, M., Moisy, C., Le Masson, E., Aoulad
953 Lafkih, Z., Vallé, C., Ygorra, B., & Baghdadi, N. (2020). Global Monitoring of the Vegetation Dynamics from
954 the Vegetation Optical Depth (VOD): A Review. *Remote Sensing, 12*

955 Freeman, A., & Durden, S.L. (1993). Three-component scattering model to describe polarimetric SAR data. In,
956 *Radar Polarimetry* (pp. 213-224): SPIE

957 Fung, A., & Eom, H. (1985). A Comparison between Active and Passive Sensing of Soil Moisture from
958 Vegetated Terrains. *IEEE Transactions on Geoscience and Remote Sensing, GE-23*, 768-775

959 Fuster, B., Sánchez-Zapero, J., Camacho, F., García-Santos, V., Verger, A., Lacaze, R., Weiss, M., Baret, F., &
960 Smets, B. (2020). Quality Assessment of PROBA-V LAI, fAPAR and fCOVER Collection 300 m Products of
961 Copernicus Global Land Service. *Remote Sensing, 12*

962 Grant, J.P., Wigneron, J.P., De Jeu, R.A.M., Lawrence, H., Mialon, A., Richaume, P., Al Bitar, A., Drusch, M.,
963 van Marle, M.J.E., & Kerr, Y. (2016). Comparison of SMOS and AMSR-E vegetation optical depth to four
964 MODIS-based vegetation indices. *Remote Sensing of Environment, 172*, 87-100

965 Grippa, M., & Woodhouse, I.H. (2003). Retrieval of bare soil and vegetation parameters from wind
966 scatterometer measurements over three different climatic regions. *Remote Sensing of Environment, 84*, 16-24

967 Gu, Y., Hunt, E., Wardlow, B., Basara, J.B., Brown, J.F., & Verdin, J.P. (2008). Evaluation of MODIS NDVI
968 and NDWI for vegetation drought monitoring using Oklahoma Mesonet soil moisture data. *Geophysical*
969 *Research Letters, 35*

970 Guyon, I., Weston, J., Barnhill, S., & Vapnik, V. (2002). Gene selection for cancer classification using support
971 vector machines. *Machine Learning, 46*, 389-422

972 Hahn, S., Reimer, C., Vreugdenhil, M., Melzer, T., & Wagner, W. (2017). Dynamic Characterization of the
973 Incidence Angle Dependence of Backscatter Using Metop ASCAT. *IEEE Journal of Selected Topics in Applied*
974 *Earth Observations and Remote Sensing, 10*, 2348-2359

975 Hengl, T., Mendes de Jesus, J., Heuvelink, G.B., Ruiperez Gonzalez, M., Kilibarda, M., Blagotic, A.,
976 Shangguan, W., Wright, M.N., Geng, X., Bauer-Marschallinger, B., Guevara, M.A., Vargas, R., MacMillan,
977 R.A., Batjes, N.H., Leenaars, J.G., Ribeiro, E., Wheeler, I., Mantel, S., & Kempen, B. (2017). SoilGrids250m:
978 Global gridded soil information based on machine learning. *PLoS One, 12*, e0169748

979 Hengl, T., Nussbaum, M., Wright, M.N., Heuvelink, G.B.M., & Graler, B. (2018). Random forest as a generic
980 framework for predictive modeling of spatial and spatio-temporal variables. *PeerJ, 6*, e5518

981 Hosseini, M., McNairn, H., Merzouki, A., & Pacheco, A. (2015). Estimation of Leaf Area Index (LAI) in corn
982 and soybeans using multi-polarization C- and L-band radar data. *Remote Sensing of Environment, 170*, 77-89

983 Imaoka, K., Maeda, T., Kachi, M., Kasahara, M., Ito, N., & Nakagawa, K. (2012). Status of AMSR2 instrument
984 on GCOM-W1. In, *Earth Observing Missions and Sensors: Development, Implementation, and Characterization*
985 *II* (p. 852815): International Society for Optics and Photonics

986 Kerr, Y.H., Waldteufel, P., Richaume, P., Wigneron, J.P., Ferrazzoli, P., Mahmoodi, A., Al Bitar, A., Cabot, F.,
987 Gruhier, C., Juglea, S.E., Leroux, D., Mialon, A., & Delwart, S. (2012). The SMOS Soil Moisture Retrieval
988 Algorithm. *IEEE Transactions on Geoscience and Remote Sensing, 50*, 1384-1403

Kerr, Y.H., Waldteufel, P., Wigneron, J.-P., Delwart, S., Cabot, F., Boutin, J., Escorihuela, M.-J., Font, J., Reul, N., Gruhier, C., Juglea, S.E., Drinkwater, M.R., Hahne, A., Martín-Neira, M., & Mecklenburg, S. (2010). The SMOS Mission: New Tool for Monitoring Key Elements ofthe Global Water Cycle. *Proceedings of the IEEE, 98*, 666-687

Konings, A.G., Piles, M., Das, N., & Entekhabi, D. (2017). L-band vegetation optical depth and effective scattering albedo estimation from SMAP. *Remote Sensing of Environment, 198*, 460-470

Konings, A.G., Piles, M., Rötzer, K., McColl, K.A., Chan, S.K., & Entekhabi, D. (2016). Vegetation optical depth and scattering albedo retrieval using time series of dual-polarized L-band radiometer observations. *Remote Sensing of Environment, 172*, 178-189

Kurum, M. (2013). Quantifying scattering albedo in microwave emission of vegetated terrain. *Remote Sensing of Environment, 129*, 66-74

Lal, P., Singh, G., Das, N.N., Colliander, A., & Entekhabi, D. (2022). Assessment of ERA5-Land Volumetric Soil Water Layer Product Using In Situ and SMAP Soil Moisture Observations. *Ieee Geoscience and Remote Sensing Letters, 19*, 1-5

Lang, N., Kalischek, N., Armston, J., Schindler, K., Dubayah, R., & Wegner, J.D. (2022). Global canopy height regression and uncertainty estimation from GEDI LIDAR waveforms with deep ensembles. *Remote Sensing of Environment, 268*

Li, X., Wigneron, J.-P., Fan, L., Frappart, F., Yueh, S.H., Colliander, A., Ebtehaj, A., Gao, L., Fernandez-Moran, R., Liu, X., Wang, M., Ma, H., Moisy, C., & Ciais, P. (2022). A new SMAP soil moisture and vegetation optical depth product (SMAP-IB): Algorithm, assessment and inter-comparison. *Remote Sensing of Environment, 271*

Li, X.J., Al-Yaari, A., Schwank, M., Fan, L., Frappart, F., Swenson, J., & Wigneron, J.P. (2020). Compared performances of SMOS-IC soil moisture and vegetation optical depth retrievals based on Tau-Omega and Two-Stream microwave emission models. *Remote Sensing of Environment, 236*

Li, X.J., Wigneron, J.P., Frappart, F., Fan, L., Ciais, P., Fensholt, R., Entekhabi, D., Brandt, M., Konings, A.G., Liu, X.Z., Wang, M.J., Al-Yaari, A., & Moisy, C. (2021). Global-scale assessment and inter-comparison of recently developed/reprocessed microwave satellite vegetation optical depth products. *Remote Sensing of Environment, 253*

Li, Y., Zhang, W., Schwalm, C.R., Gentine, P., Smith, W.K., Ciais, P., Kimball, J.S., Gazol, A., Kannenberg, S.A., Chen, A., Piao, S., Liu, H., Chen, D., & Wu, X. (2023). Widespread spring phenology effects on drought recovery of Northern Hemisphere ecosystems. *Nature Climate Change*

Liao, Z., Liu, X., van Dijk, A., Yue, C., & He, B. (2022). Continuous woody vegetation biomass estimation based on temporal modeling of Landsat data. *International Journal of Applied Earth Observation and Geoinformation, 110*

Lievens, H., Brangers, I., Marshall, H.-P., Jonas, T., Olefs, M., & De Lannoy, G. (2021). Sentinel-1 snow depth retrieval at sub-kilometer resolution over the European Alps

Lievens, H., Martens, B., Verhoest, N.E.C., Hahn, S., Reichle, R.H., & Miralles, D.G. (2017). Assimilation of global radar backscatter and radiometer brightness temperature observations to improve soil moisture and land evaporation estimates. *Remote Sensing of Environment, 189*, 194-210

Lin, W., Wu, Z., Lin, L., Wen, A., & Li, J. (2017). An Ensemble Random Forest Algorithm for Insurance Big Data Analysis. *IEEE Access, 5*, 16568-16575

Link, M., Jagdhuber, T., Ferrazzoli, P., Guerriero, L., & Entekhabi, D. (2021). Relationship Between Active and Passive Microwave Signals Over Vegetated Surfaces. *IEEE Transactions on Geoscience and Remote Sensing*, 1-15

Liu, P.-W., Judge, J., DeRoo, R.D., England, A.W., Bongiovanni, T., & Luke, A. (2016). Dominant backscattering mechanisms at L-band during dynamic soil moisture conditions for sandy soils. *Remote Sensing of Environment, 178*, 104-112

Liu, X., Wigneron, J.P., Frappart, F., Baghdadi, N., Zribi, M., Jagdhuber, T., Ciais, P., Li, X., Wang, M., Fan, L., Ygorra, B., Ma, H., Xing, Z., Al-Yaari, A., Fernandez-Moran, R., & Moisy, C. (2021a). First Retrievals of ASCAT IB VOD (Vegetation Optical Depth) at Global Scale. In, *2021 IEEE International Geoscience and Remote Sensing Symposium IGARSS* (pp. 6403-6406)

Liu, X.Z., Wigneron, J.P., Fan, L., Frappart, F., Ciais, P., Baghdadi, N., Zribi, M., Jagdhuber, T., Li, X.J., Wang, M.J., Bai, X.J., & Moisy, C. (2021b). ASCAT IB: A radar-based vegetation optical depth retrieved from the ASCAT scatterometer satellite. *Remote Sensing of Environment, 264*

Liu, Y.Y., de Jeu, R.A.M., McCabe, M.F., Evans, J.P., & van Dijk, A.I.J.M. (2011). Global long-term passive microwave satellite-based retrievals of vegetation optical depth. *Geophysical Research Letters, 38*, n/a-n/a

Liu, Y.Y., van Dijk, A.I.J.M., McCabe, M.F., Evans, J.P., & de Jeu, R.A.M. (2013). Global vegetation biomass change (1988-2008) and attribution to environmental and human drivers. *Global Ecology and Biogeography, 22*, 692-705

Lyons, D.S., Dobrowski, S.Z., Holden, Z.A., Maneta, M.P., & Sala, A. (2021). Soil moisture variation drives canopy water content dynamics across the western U.S. *Remote Sensing of Environment, 253*

Macelloni, G., Paloscia, S., Pampaloni, P., Marliani, F., & Gai, M. (2001). The relationship between the backscattering coefficient and the biomass of narrow and broad leaf crops. *IEEE Transactions on Geoscience and Remote Sensing, 39*, 873-884

Magagi, R.D., & Kerr, Y.H. (1997). Retrieval of soil moisture and vegetation characteristics by use of ERS-1 wind scatterometer over arid and semi-arid areas. *Journal of Hydrology, 188-189*, 361-384

McColl, K.A., Entekhabi, D., & Piles, M. (2014). Uncertainty Analysis of Soil Moisture and Vegetation Indices Using Aquarius Scatterometer Observations. *IEEE Transactions on Geoscience and Remote Sensing, 52*, 4259-4272

Meroni, M., d'Andrimont, R., Vrieling, A., Fasbender, D., Lemoine, G., Rembold, F., Seguini, L., & Verhegghen, A. (2021). Comparing land surface phenology of major European crops as derived from SAR and multispectral data of Sentinel-1 and -2. *Remote Sens Environ, 253*, 112232

Moesinger, L., Dorigo, W., de Jeu, R., van der Schalie, R., Scanlon, T., Teubner, I., & Forkel, M. (2020). The global long-term microwave Vegetation Optical Depth Climate Archive (VODCA). *Earth System Science Data, 12*, 177-196

Muñoz-Sabater, J., Dutra, E., Agustí-Panareda, A., Albergel, C., Arduini, G., Balsamo, G., Boussetta, S., Choulga, M., Harrigan, S., Hersbach, H., Martens, B., Miralles, D.G., Piles, M., Rodríguez-Fernández, N.J., Zsoter, E., Buontempo, C., & Thépaut, J.-N. (2021). ERA5-Land: a state-of-the-art global reanalysis dataset for land applications. *Earth System Science Data, 13*, 4349-4383

Neumann, M., Ferro-Famil, L., & Reigber, A. (2010). Estimation of Forest Structure, Ground, and Canopy Layer Characteristics From Multibaseline Polarimetric Interferometric SAR Data. *IEEE Transactions on Geoscience and Remote Sensing, 48*, 1086-1104

O'Neill, P.E., Njoku, E.G., Jackson, T.J., Chan, S., & Bindlish, R. (2015). SMAP Algorithm Theoretical Basis Document: Level 2 & 3 Soil Moisture (Passive) Data Products. In

Owe, M., de Jeu, R., & Holmes, T. (2008). Multisensor historical climatology of satellite-derived global land surface moisture. *Journal of Geophysical Research, 113*

Pedregosa, F., Varoquaux, G., Gramfort, A., Michel, V., Thirion, B., Grisel, O., Blondel, M., Prettenhofer, P., Weiss, R., Dubourg, V., Vanderplas, J., Passos, A., Cournapeau, D., Brucher, M., Perrot, M., & Duchesnay, E. (2011). Scikit-learn: Machine Learning in Python. *Journal of Machine Learning Research, 12*, 2825-2830

Pfeil, I., Vreugdenhil, M., Hahn, S., Wagner, W., Strauss, P., & Blöschl, G. (2018). Improving the Seasonal Representation of ASCAT Soil Moisture and Vegetation Dynamics in a Temperate Climate. *Remote Sensing, 10*, 1788

Piles, M., McColl, K.A., Entekhabi, D., Das, N., & Pablos, M. (2015). Sensitivity of Aquarius Active and Passive Measurements Temporal Covariability to Land Surface Characteristics. *IEEE Transactions on Geoscience and Remote Sensing, 53*, 4700-4711

Potapov, P., Li, X., Hernandez-Serna, A., Tyukavina, A., Hansen, M.C., Kommareddy, A., Pickens, A., Turubanova, S., Tang, H., Silva, C.E., Armston, J., Dubayah, R., Blair, J.B., & Hofton, M. (2020). Mapping global forest canopy height through integration of GEDI and Landsat data. *Remote Sensing of Environment*

Pouladi, N., Møller, A.B., Tabatabai, S., & Greve, M.H. (2019). Mapping soil organic matter contents at field level with Cubist, Random Forest and kriging. *Geoderma, 342*, 85-92

Prigent, C., Jimenez, C., Dinh, L.A., Frappart, F., Gentine, P., Wigneron, J.P., & Munchak, J. (2022). Diurnal and Seasonal Variations of Passive and Active Microwave Satellite Observations Over Tropical Forests. *Journal of Geophysical Research: Biogeosciences, 127*

Quast, R., Albergel, C., Calvet, J.-C., & Wagner, W. (2019). A Generic First-Order Radiative Transfer Modelling Approach for the Inversion of Soil and Vegetation Parameters from Scatterometer Observations. *Remote Sensing, 11*

Rodríguez-Fernández, N.J., Mialon, A., Mermoz, S., Bouvet, A., Richaume, P., Al Bitar, A., Al-Yaari, A., Brandt, M., Kaminski, T., Le Toan, T., Kerr, Y.H., & Wigneron, J.-P. (2018a). An evaluation of SMOS L-band vegetation optical depth (L-VOD) data sets: high sensitivity of L-VOD to above-ground biomass in Africa. *Biogeosciences, 15*, 4627-4645

Rodríguez-Fernández, N.J., Mialon, A., Mermoz, S., Bouvet, A., Richaume, P., Al Bitar, A., Al-Yaari, A., Brandt, M., Kaminski, T., Le Toan, T., Kerr, Y.H., & Wigneron, J.-P. (2018b). The high sensitivity of SMOS L-Band vegetation optical depth to biomass. *Biogeosciences Discussions*, 1-20

Saatchi, S.S., Harris, N.L., Brown, S., Lefsky, M., Mitchard, E.T., Salas, W., Zutta, B.R., Buermann, W., Lewis, S.L., Hagen, S., Petrova, S., White, L., Silman, M., & Morel, A. (2011). Benchmark map of forest carbon stocks in tropical regions across three continents. *Proc Natl Acad Sci U S A, 108*, 9899-9904

Santoro, M., & Cartus, O. (2019). ESA Biomass Climate Change Initiative (Biomass_cci): Global datasets of forest above-ground biomass for the year 2017, v1. In: Centre for Environmental Data Analysis

Santoro, M., Cartus, O., Wegmüller, U., Besnard, S., Carvalhais, N., Araza, A., Herold, M., Liang, J., Cavlovic, J., & Engdahl, M.E. (2022). Global estimation of above-ground biomass from spaceborne C-band scatterometer observations aided by LiDAR metrics of vegetation structure. *Remote Sensing of Environment, 279*

Schwank, M., Naderpour, R., & Mätzler, C. (2018). "Tau-Omega"- and Two-Stream Emission Models Used for Passive L-Band Retrievals: Application to Close-Range Measurements over a Forest. *Remote Sensing, 10*

Shamambo, D.C., Bonan, B., Calvet, J.-C., Albergel, C., & Hahn, S. (2019). Interpretation of ASCAT Radar Scatterometer Observations Over Land: A Case Study Over Southwestern France. *Remote Sensing, 11*

Shan, X., Steele-Dunne, S., Huber, M., Hahn, S., Wagner, W., Bonan, B., Albergel, C., Calvet, J.-C., Ku, O., & Georgievska, S. (2022). Towards constraining soil and vegetation dynamics in land surface models: Modeling ASCAT backscatter incidence-angle dependence with a Deep Neural Network. *Remote Sensing of Environment, 279*

Srivastava, P.K., Pandey, V., Suman, S., Gupta, M., & Islam, T. (2016). Available Data Sets and Satellites for Terrestrial Soil Moisture Estimation, 29-44

Steele-Dunne, S.C., Hahn, S., Wagner, W., & Vreugdenhil, M. (2019). Investigating vegetation water dynamics and drought using Metop ASCAT over the North American Grasslands. *Remote Sensing of Environment, 224*, 219-235

Stone, M. (1974). Cross-Validatory Choice and Assessment of Statistical Predictions. *Journal of the Royal Statistical Society: Series B (Methodological), 36*, 111-133

Sulla-Menashe, D., Gray, J.M., Abercrombie, S.P., & Friedl, M.A. (2019). Hierarchical mapping of annual global land cover 2001 to present: The MODIS Collection 6 Land Cover product. *Remote Sensing of Environment, 222*, 183-194

Tao, S., Chave, J., Frison, P.L., Le Toan, T., Ciais, P., Fang, J., Wigneron, J.P., Santoro, M., Yang, H., Li, X., Labriere, N., & Saatchi, S. (2022). Increasing and widespread vulnerability of intact tropical rainforests to repeated droughts. *Proc Natl Acad Sci U S A, 119*, e2116626119

Teubner, I.E., Forkel, M., Jung, M., Liu, Y.Y., Miralles, D.G., Parinussa, R., van der Schalie, R., Vreugdenhil, M., Schwalm, C.R., Tramontana, G., Camps-Valls, G., & Dorigo, W.A. (2018). Assessing the relationship between microwave vegetation optical depth and gross primary production. *International Journal of Applied Earth Observation and Geoinformation, 65*, 79-91

Tian, F., Brandt, M., Liu, Y.Y., Verger, A., Tagesson, T., Diouf, A.A., Rasmussen, K., Mbow, C., Wang, Y., & Fensholt, R. (2016). Remote sensing of vegetation dynamics in drylands: Evaluating vegetation optical depth (VOD) using AVHRR NDVI and in situ green biomass data over West African Sahel. *Remote Sensing of Environment, 177*, 265-276

Ulaby, F., Batlivala, P., & Dobson, M. (1978). Microwave Backscatter Dependence on Surface Roughness, Soil Moisture, and Soil Texture: Part I-Bare Soil. *IEEE Transactions on Geoscience Electronics, 16*, 286-295

Ulaby, F.T., Sarabandi, K., McDonald, K., Whitt, M., & Dobson, M.C. (1990). Michigan microwave canopy scattering model. *International Journal of Remote Sensing, 11*, 1223-1253

Urbazaev, M., Thiel, C., Cremer, F., Dubayah, R., Migliavacca, M., Reichstein, M., & Schmullius, C. (2018). Estimation of forest aboveground biomass and uncertainties by integration of field measurements, airborne LiDAR, and SAR and optical satellite data in Mexico. *Carbon Balance Manag, 13*, 5

van der Schalie, R., de Jeu, R.A.M., Kerr, Y.H., Wigneron, J.P., Rodríguez-Fernández, N.J., Al-Yaari, A., Parinussa, R.M., Mecklenburg, S., & Drusch, M. (2017). The merging of radiative transfer based surface soil moisture data from SMOS and AMSR-E. *Remote Sensing of Environment, 189*, 180-193

Verhoest, N.E., Lievens, H., Wagner, W., Alvarez-Mozos, J., Moran, M.S., & Mattia, F. (2008). On the Soil Roughness Parameterization Problem in Soil Moisture Retrieval of Bare Surfaces from Synthetic Aperture Radar. *Sensors (Basel), 8*, 4213-4248

Vittucci, C., Ferrazzoli, P., Richaume, P., & Kerr, Y. (2017). Effective Scattering Albedo of Forests Retrieved by SMOS and a Three-Parameter Algorithm. *Ieee Geoscience and Remote Sensing Letters, 14*, 2260-2264

Vittucci, C., Vaglio Laurin, G., Tramontana, G., Ferrazzoli, P., Guerriero, L., & Papale, D. (2019). Vegetation optical depth at L-band and above ground biomass in the tropical range: Evaluating their relationships at continental and regional scales. *International Journal of Applied Earth Observation and Geoinformation, 77*, 151-161

Vreugdenhil, M., Dorigo, W.A., Wagner, W., de Jeu, R.A.M., Hahn, S., & van Marle, M.J.E. (2016). Analyzing the Vegetation Parameterization in the TU-Wien ASCAT Soil Moisture Retrieval. *IEEE Transactions on Geoscience and Remote Sensing, 54*, 3513-3531

Vreugdenhil, M., Hahn, S., Melzer, T., BauerMarschallinger, B., Reimer, C., Dorigo, W.A., & Wagner, W. (2017). Assessing Vegetation Dynamics Over Mainland Australia With Metop ASCAT. *IEEE Journal of Selected Topics in Applied Earth Observations and Remote Sensing, 10*, 2240-2248

Wagner, W., Hahn, S., Kidd, R., Melzer, T., Bartalis, Z., Hasenauer, S., Figa-Saldaña, J., de Rosnay, P., Jann, A., Schneider, S., Komma, J., Kubu, G., Brugger, K., Aubrecht, C., Züger, J., Gangkofner, U., Kienberger, S., Brocca, L., Wang, Y., Blöschl, G., Eitzinger, J., & Steinnocher, K. (2013). The ASCAT Soil Moisture Product: A Review of its Specifications, Validation Results, and Emerging Applications. *Meteorologische Zeitschrift, 22*, 5-33

Wagner, W., Lemoine, G., Borgeaud, M., & Rott, H. (1999). A study of vegetation cover effects on ERS scatterometer data. *IEEE Transactions on Geoscience and Remote Sensing, 37*, 938-948

Wagner, W., Lindorfer, R., Melzer, T., Hahn, S., Bauer-Marschallinger, B., Morrison, K., Calvet, J.-C., Hobbs, S., Quast, R., Greimeister-Pfeil, I., & Vreugdenhil, M. (2022). Widespread occurrence of anomalous C-band backscatter signals in arid environments caused by subsurface scattering. *Remote Sensing of Environment, 276*

Wang, H., Wigneron, J.-P., Ciais, P., Yao, Y., Fan, L., Liu, X., Li, X., Green, J.K., Tian, F., Tao, S., Li, W., Frappart, F., Albergel, C., Wang, M., & Li, S. (2023). Seasonal variations in vegetation water content retrieved from microwave remote sensing over Amazon intact forests. *Remote Sensing of Environment, 285*

Wang, M., Fan, L., Frappart, F., Ciais, P., Sun, R., Liu, Y., Li, X., Liu, X., Moisy, C., & Wigneron, J.-P. (2021a). An alternative AMSR2 vegetation optical depth for monitoring vegetation at large scales. *Remote Sensing of Environment, 263*

Wang, M., Wigneron, J.-P., Sun, R., Fan, L., Frappart, F., Tao, S., Chai, L., Li, X., Liu, X., Ma, H., Moisy, C., & Ciais, P. (2021b). A consistent record of vegetation optical depth retrieved from the AMSR-E and AMSR2 X-band observations. *International Journal of Applied Earth Observation and Geoinformation, 105*

Wang, N., Peng, J., Xue, J., Zhang, X., Huang, J., Biswas, A., He, Y., & Shi, Z. (2022). A framework for determining the total salt content of soil profiles using time-series Sentinel-2 images and a random forest-temporal convolution network. *Geoderma, 409*

Wigneron, J.-P., Li, X., Frappart, F., Fan, L., Al-Yaari, A., De Lannoy, G., Liu, X., Wang, M., Le Masson, E., & Moisy, C. (2021). SMOS-IC data record of soil moisture and L-VOD: Historical development, applications and perspectives. *Remote Sensing of Environment, 254*

Wigneron, J.P., Fan, L., Ciais, P., Bastos, A., Brandt, M., Chave, J., Saatchi, S., Baccini, A., & Fensholt, R. (2020). Tropical forests did not recover from the strong 2015-2016 El Nino event. *Sci Adv, 6*, eaay4603

Wigneron, J.P., Ferrazzoli, P., Calvet, J.C., & Bertuzzi, P. (1999). A parametric study on passive and active microwave observations over a soybean crop. *IEEE Transactions on Geoscience and Remote Sensing, 37*, 2728-2733

Wigneron, J.P., Jackson, T.J., O'Neill, P., De Lannoy, G., de Rosnay, P., Walker, J.P., Ferrazzoli, P., Mironov, V., Bircher, S., Grant, J.P., Kurum, M., Schwank, M., Munoz-Sabater, J., Das, N., Royer, A., Al-Yaari, A., Al Bitar, A., Fernandez-Moran, R., Lawrence, H., Mialon, A., Parrens, M., Richaume, P., Delwart, S., & Kerr, Y. (2017). Modelling the passive microwave signature from land surfaces: A review of recent results and application to the L-band SMOS & SMAP soil moisture retrieval algorithms. *Remote Sensing of Environment, 192*, 238-262

Wigneron, J.P., Kerr, Y., Waldteufel, P., Saleh, K., Escorihuela, M.J., Richaume, P., Ferrazzoli, P., de Rosnay, P., Gurney, R., Calvet, J.C., Grant, J.P., Guglielmetti, M., Hornbuckle, B., Mätzler, C., Pellarin, T., & Schwank, M. (2007). L-band Microwave Emission of the Biosphere (L-MEB) Model: Description and calibration against experimental data sets over crop fields. *Remote Sensing of Environment, 107*, 639-655

Wigneron, J.P., Waldteufel, P., Chanzy, A., Calvet, J.C., & Kerr, Y. (2000). Two-Dimensional Microwave Interferometer Retrieval Capabilities over Land Surfaces (SMOS Mission). *Remote Sensing of Environment, 73*, 270-282

Xing, Z., Fan, L., Zhao, L., De Lannoy, G., Frappart, F., Peng, J., Li, X., Zeng, J., Al-Yaari, A., Yang, K., Zhao, T., Shi, J., Wang, M., Liu, X., Hu, G., Xiao, Y., Du, E., Li, R., Qiao, Y., Shi, J., Wen, J., Ma, M., & Wigneron, J.-P. (2021). A first assessment of satellite and reanalysis estimates of surface and root-zone soil moisture over the permafrost region of Qinghai-Tibet Plateau. *Remote Sensing of Environment, 265*

Zhou, Z., Fan, L., De Lannoy, G.D., Liu, X., Peng, J., Bai, X., Frappart, F., Baghdadi, N., Xing, Z., Li, X., Ma, M., Li, X., Che, T., Geng, L., & Wigneron, J.-P. (2022). Retrieval of High-Resolution Vegetation Optical Depth from Sentinel-1 Data over a Grassland Region in the Heihe River Basin. *Remote Sensing, 14*

Zribi, M., Muddu, S., Bousbih, S., Al Bitar, A., Tomer, S.K., Baghdadi, N., & Bandyopadhyay, S. (2019). Analysis of L-Band SAR Data for Soil Moisture Estimations over Agricultural Areas in the Tropics. *Remote Sensing, 11*